

Deformations and magnetic rotations in the ^{60}Ni nucleus

D. A. Torres* and F. Cristancho

*Departamento de Física, Universidad Nacional de Colombia, Bogotá, Colombia*L.-L. Andersson, E. K. Johansson, D. Rudolph, C. Fahlander, J. Ekman,[†] and R. du Rietz[‡]*Department of Physics, Lund University, S-22100 Lund, Sweden*C. Andreoiu[§]*Department of Physics, University of Guelph, Guelph, Ontario, Canada N1G 2W1*

M. P. Carpenter, D. Seweryniak, and S. Zhu

*Physics Division, Argonne National Laboratory, Argonne, Illinois 60493, USA*R. J. Charity, C. J. Chiara,^{||} C. Hoel, O. L. Pechenaya,

W. Reviol, D. G. Sarantites, and L. G. Sobotka

Chemistry Department, Washington University, St Louis, Missouri 63130, USA

C. Baktash and C.-H. Yu

Physics Division, Oak Ridge National Laboratory, Oak Ridge, Tennessee 37831, USA

B. G. Carlsson and I. Ragnarsson

Department of Mathematical Physics, Lund Institute of Technology, S-22100 Lund, Sweden

(Received 6 June 2008; published 25 November 2008)

Data from three experiments using the heavy-ion fusion evaporation-reaction $^{36}\text{Ar}+^{28}\text{Si}$ have been combined to study high-spin states in the residual nucleus ^{60}Ni , which is populated via the evaporation of four protons from the compound nucleus ^{64}Ge . The GAMMASPHERE array was used for all the experiments in conjunction with a 4π charged-particle detector arrays (MICROBALL, LUWUSIA) and neutron detectors (NEUTRON SHELL) to allow for the detection of γ rays in coincidence with the evaporated particles. An extended ^{60}Ni level scheme is presented, comprising more than 270 γ -ray transitions and 110 excited states. Their spins and parities have been assigned via directional correlations of γ rays emitted from oriented states. Spherical shell-model calculations in the fp -shell characterize some of the low-spin states, while the experimental results of the rotational bands are analyzed with configuration-dependent cranked Nilsson-Strutinsky calculations.

DOI: [10.1103/PhysRevC.78.054318](https://doi.org/10.1103/PhysRevC.78.054318)

PACS number(s): 21.60.Cs, 23.20.Lv, 23.20.En, 27.50.+e

I. INTRODUCTION

During recent years the mass $A \approx 60$ region has seen an extensive and systematic study of high-spin states, and a plethora of different phenomena has been investigated. To name some of them: deformation and superdeformation in ^{59}Cu [1] and ^{62}Zn [2,3]; prompt discrete proton and α -particle

decay from superdeformed bands to spherical states in ^{58}Cu [4,5], ^{59}Cu [6], ^{56}Ni [7,8], ^{58}Ni [9], and ^{60}Zn [10]; the decay-out of the superdeformed bands through doorway states in ^{59}Cu [11]; interacting states at record heights of excitation energy and rotational frequency [12]; triaxial deformation; band termination; and bands with strong dipole transitions [13,14]. All of these phenomena have provided a very interesting picture for this light mass region and have simultaneously raised several new questions, which the experiments described below are addressing. In the specific case of ^{60}Ni , theoretical calculations [15,16] predict that around $(Z, N) = (28, 28)$ $M1$ rotational bands may be observable. The same kind of predictions have been experimentally verified in heavier mass regions [17,18]. In fact, ^{60}Ni with four neutrons outside the double magic ^{56}Ni core presents at high excitation energy and high spin favorable conditions for a nucleus to be able of showing magnetic rotation, particles and holes in high- j shells: $1g_{9/2}$ neutrons and $1f_{7/2}$ proton-holes. It is then to be investigated whether the interplay between collective and single-particle phenomena allows the formation of structures featuring magnetic rotation.

*Present address: School of Engineering and Science, University of the West of Scotland, High Street, Paisley, PA1 2BE, UK; Diego.Torres@uws.ac.uk

[†]Present address: Technology and Society, Malmö University, S-205 06 Malmö, Sweden.

[‡]Present address: Department of Nuclear Physics, Research School of Physical Science and Engineering, The Australian National University Canberra, ACT 0200, Australia.

[§]Present address: Chemistry Department, Simon Fraser University, 8888 University Drive, Burnaby, BC, V5A 1S6, Canada.

^{||}Present address: Nuclear Engineering Division, Argonne National Laboratory, Argonne, Illinois 60439, USA.

On the other hand, structurally speaking, the characteristics of the low-energy low-spin excitations are marked by the interplay between the $2p_{3/2}$, $1f_{5/2}$, and $2p_{1/2}$ shells with the $1g_{9/2}$ shell expected to determine the structure of deformed states at high excitation energy and angular momentum as in other nearby nuclei [1,6]. Regarding previous research, the low spin states of ^{60}Ni have been investigated mainly by (n, γ) reactions [19] whereas heavy-ion reactions have been used to investigate structural properties of its high-spin states to some 10 MeV excitation energy [20–24]. The higher excited states observed up to a tentative spin of $I^\pi = 15^+$ and excitation energy of 12.3 MeV [16,20] show already collective character whose nature is to be investigated.

The present paper may be viewed as an extensive high-spin spectroscopy study of ^{60}Ni . Section II briefly describes the experiments and applied analysis techniques. In Sec. III the extensive level scheme is discussed in detail. Section IV provides an interpretation of the low-lying positive-parity states in the framework of the spherical shell model and an analysis of the rotational structures with the configuration-dependent cranked Nilsson-Strutinsky (CNS) approach. The conclusions are presented in Sec. V.

II. EXPERIMENTAL PROCEDURE AND ANALYSIS

The experiments were performed at Argonne National Laboratory (GSFMA138 and GSFMA42) and at Lawrence Berkeley National Laboratory (GS54) using the GAMMASPHERE array [25] in conjunction with charged-particle detectors, and neutron detectors. The Fragment Mass Analyzer (FMA) was also used for one of the experiments. In all the three experiments ^{60}Ni was produced using the fusion-evaporation reaction $^{28}\text{Si}(^{36}\text{Ar}, 4p)$; the relative cross section for the $4p$ channel is about 11% of the total fusion cross section. Hence, ^{60}Ni is one of the strongest channels, together with $^{60,61}\text{Cu}$, ^{58}Ni , and ^{57}Co . The $4p$ -selection exclude these strong channel, and provides a clear analysis environment to an unambiguous determination of in particular the weakest structures and/or decay-out branches. It is important to provide extensive and as complete as possible decay schemes in order to be sensitive to exotic decay modes, for example prompt particle decays, and unexpected excitational modes.

In the GSFMA138 experiment, a nominally 0.2-mg/cm² thin ^{28}Si target (the detailed kinematic correction for the γ -rays indicates a target thickness twice as large as expected [26]) was evaporated onto a 1.1 mg/cm² Ta foil. The Ta foil faced the beam reducing the original beam energy of 142 MeV by some 8 MeV. The Hevimet collimators were removed from the GAMMASPHERE detectors to provide on an event-by-event basis γ -ray multiplicity, k , and sum-energy, H , measurements, as well as additional selectivity by total energy (TE) conservation requirements [27]. The event trigger required the detection of at least four Compton suppressed γ -rays or three Compton suppressed γ -rays plus one neutron.

30 of the most forward Ge-detectors in GAMMASPHERE were replaced by the liquid-scintillator neutron detector array NEUTRON SHELL [28]. Evaporated charged particles were detected in the new $3\pi \Delta E$ - E silicon strip telescope array

LUWUSIA [8,29], which replaced the forward seven rings of the MICROBALL [30]. The two most backward rings of the MICROBALL were used to complete the solid angle in the charged-particle detection. Each of the silicon telescopes in the LUWUSIA array consisted of a ΔE counter with a thickness of $\sim 65 \mu\text{m}$ in front of an E detector of thickness ~ 1 mm. Each ΔE element was $50 \times 50 \text{ mm}^2$ and each E element was $60 \times 60 \text{ mm}^2$ in size and separated into 16 strips. The array is formed by four telescopes in a forward wall (the so-called Silicon Wall), and four telescopes forming a central box (the so-called Silicon Box) around the beam. The arrangement gives rise to $8 \times 16 \times 16 = 2048$ pixels of approximately $3 \times 3 \text{ mm}^2$ size. Due to the geometrical limit set by the two last rings of MICROBALL and by the Silicon Box only some 1800 pixels are active in the LUWUSIA array.

For the GSFMA42 experiment an argon beam of a nominal energy of 148 MeV was used. The 0.42 mg/cm² thin target layer was sputtered onto a 1.0 mg/cm² gold support foil, which faced the beam. The setup included 20 neutron scintillation detectors replacing the 20 most forward Ge-detectors. The Hevimet collimators in front of the Ge-detectors were removed. Evaporated charged particles were detected in MICROBALL and in the Silicon Wall, which replaced the three forward rings of MICROBALL [4]. Around 800 pixels were available for the detection of particles coming from the reaction site. More details about the experimental setup and the data analysis can be found in Ref. [4].

For the GS54 experiment the target arrangement was essentially the same as for GSFMA42. This time the beam energy was 143 MeV. Neutrons were detected with scintillation detectors replacing the 15 most forward Ge-detectors. Charged particles were detected using the MICROBALL array.

An event-by-event kinematical reconstruction of the momenta of the recoil nuclei [31] was performed for all the three experiments. This allowed for a more accurate Doppler shift correction of the γ -ray energies (E_γ), leading to a significantly improved γ -ray energy resolution, especially for the GSFMA42 and, even more, the GSFMA138 experiment, for which highly pixelized silicon strip detectors were used. As an example, in the GSFMA138 experiment a FWHM of ~ 13 keV for a γ -ray transition of ~ 3 MeV for the $2\alpha 1p$ evaporation channel was obtained [26]. This is practically the limit imposed by the Ge detector opening angle.

The events were sorted and the results were combined offline into various γ -ray energy projections, E_γ - E_γ matrices, and E_γ - E_γ - E_γ cubes subject to appropriate evaporated particle conditions, i.e., proton identification and TE-gating. The statistics obtained allowed us to reach an intensity resolution of 1 per 1000. Analysis of the events employed the RADWARE software package [32] and the spectrum-analysis code Tv [33]. The main result of the TE-gated $\gamma\gamma$ and $\gamma\gamma\gamma$ -coincidence analysis is the high-spin excitation scheme of ^{60}Ni , shown in Fig. 1. It is based on coincidence relations, intensity balances, and energy relations. The level energies, the corresponding depopulating γ rays, their relative intensities, angular-correlation ratios, and resulting spin-parity assignments are summarized in Table I.

The assignment of the multipolarities is based on directional correlations from oriented states (DCO ratios).

TABLE I. The energies of excited states in ^{60}Ni together with the transition energies and relative intensities of the γ rays placed in the level scheme, angular correlation ratios, and the spins and parities of the initial and final states of the γ transitions. Quantities in italic correspond to previously reported level energies or γ -ray energy transitions.

E_x [keV]	E_γ [keV]	I_{rel}	$R_{\text{DCO}}(30-83)$		Multipole assignment	I_i^π [\hbar]	I_f^π [\hbar]
			Gate $E2$	Gate $\Delta I = 1$			
<i>1332.6(2)</i>	<i>1332.5(2)</i>	1000(30)	1.00(4)		$E2$	2^{+a}	0^+
<i>2158.9(2)</i>	<i>826.1(2)</i>	58(3)	1.07(8)		$\Delta I = 0$	2^{+a}	2^+
	<i>2159.0(3)</i>	9(1)			$E2$	2^+	0^+
<i>2505.8(2)</i>	<i>346.8(4)</i>	2(1)			$E2$	4^{+a}	2^+
	<i>1173.2(2)</i>	820(25)	1.03(4)		$E2$	4^+	2^+
<i>2626.1(2)</i>	<i>119.6(1)</i>	12(2)			$E2/M1$	3^{+a}	4^+
	<i>467.1(1)</i>	36(2)	1.02(8)		$E2/M1$	3^+	2^+
	<i>1293.7(2)</i>	16(2)	0.56(2)		$E2/M1$	3^+	2^+
<i>3119.5(2)</i>	<i>493.4(1)</i>	12(2)	0.64(9)		$E2/M1$	4^{+a}	3^+
	613.7(3)	4(1)			$\Delta I = 0$	4^+	4^+
	<i>1787.3(3)</i>	91(4)	1.10(5)		$E2$	4^+	2^+
<i>3186.8(2)</i>	<i>680.0(1)</i>	3(1)			$E2/M1$	3^{+a}	4^+
	<i>1028.2(2)</i>	5(1)	0.63(8)		$E2/M1$	3^+	2^+
	<i>1854.0(2)</i>	3(1)			$E2/M1$	3^+	2^+
<i>3619.6(4)</i>	<i>993.7(3)</i>	3(1)			$\Delta I = 0$	3^{+a}	3^+
<i>3671.2(2)</i>	<i>1165.2(2)</i>	62(3)	0.95(4)		$\Delta I = 0$	4^{+a}	4^+
	1512.1(6)	1(1)			$E2$	4^+	2^+
<i>3730.7(2)</i>	545.0(1)	3(1)		1.12(24)	$E2/M1$	4^{+a}	3^+
	610.9(3)	3(1)			$\Delta I = 0$	4^+	4^+
	<i>1105.0(4)</i>	5(1)			$E2/M1$	4^+	3^+
	<i>1224.9(2)</i>	7(2)		1.05(9)	$\Delta I = 0$	4^+	4^+
	<i>2398.4(3)</i>	11(2)	1.04(5)		$E2$	4^+	2^+
<i>4165.6(2)</i>	494.4(2)	5(1)	0.72(11)		$E2/M1$	5^{+a}	4^+
	1044.4(2)	8(2)			$E2/M1$	5^+	4^+
	<i>1539.0(3)</i>	8(2)			$E2$	5^+	3^+
	<i>1659.6(3)</i>	57(5)	0.32(3)		$E2/M1$	5^+	4^+
<i>4186.2(3)</i>	515(1)	2(1)			($\Delta I = 0$)	(4^+)	4^+
	1560.2(4)	3(1)			($E2/M1$)	(4^+)	3^+
<i>4265.0(2)</i>	<i>1145.2(2)</i>	37(3)	1.00(8)		$E2$	6^{+a}	4^+
	<i>1759.2(3)</i>	496(16)	1.04(5)		$E2$	6^+	4^+
<i>4407.5(2)</i>	<i>241.8(1)</i>	14(2)	0.86(10)		$\Delta I = 0$	5^{+a}	5^+
	676.6(2)	31(3)			$E2/M1$	5^+	4^+
	<i>736.4(2)</i>	19(3)			$E2/M1$	5^+	4^+
	1288.3(4)	4(1)			$E2/M1$	5^+	4^+
	1781.3(3)	9(1)			$E2$	5^+	3^+
	<i>1901.7(3)</i>	15(2)			$E2/M1$	5^+	4^+
<i>4579.0(8)</i>	<i>1952.9(5)</i>	7(1)			$E2/M1$	(4^+)	3^+
<i>4985.9(2)</i>	<i>578.3(3)</i>	9(2)			$E2/M1$	6^{+a}	5^+
	<i>720.9(2)</i>	27(2)	0.98(4)		$\Delta I = 0$	6^+	6^+
	820.5(2)	7(1)		0.60(5)	$E2/M1$	6^+	5^+
	1255.8(2)	5(1)			$E2$	6^+	4^+
	<i>1314.5(2)</i>	18(2)	1.03(8)	1.34(11)	$E2$	6^+	4^+
	1867.0(3)	6(1)	1.38(34)		$E2$	6^+	4^+
	<i>2480.6(3)</i>	53(3)	0.91(7)		$E2$	6^+	4^+
<i>5014.5(3)</i>	749.5(3)	1(1)			$E1$	5^{-a}	6^+
	828.3(3)	2(1)			($E1$)	5^-	(4^+)
	848.9(1)	1(1)			$E1$	5^-	5^+
	1283.8(4)	3(1)			$E1$	5^-	4^+
	<i>1343.3(2)</i>	17(2)	0.74(6)		$E1$	5^-	4^+
	<i>1894.7(3)</i>	31(3)	0.74(6)		$E1$	5^-	4^+
	<i>2508.7(4)</i>	27(3)	0.72(8)		$E1$	5^-	4^+
<i>5148.4(3)</i>	<i>740.9(2)</i>	42(4)	0.81(6)		$E2/M1$	6^{+a}	5^+
	883.5(1)	12(1)	1.08(5)		$\Delta I = 0$	6^+	6^+

TABLE I. (*Continued.*)

E_x [keV]	E_γ [keV]	I_{rel}	$R_{\text{DCO}}(30-83)$		Multipole assignment	I_i^π [\hbar]	I_f^π [\hbar]
			Gate $E2$	Gate $\Delta I = 1$			
	982.9(3)	5(1)			$E2/M1$	6^+	5^+
	1477.3(4)	2(1)			$E2$	6^{+a}	4^+
	2029.0(5)	3(1)	1.06(38)		$E2$	6^+	4^+
	2643.0(4)	25(3)	0.95(9)		$E2$	6^+	4^+
5236.7(8)	2116.0(1)	10(1)	0.56(10)		$\Delta I = 1$	$5^{(+)}$	4^+
5348.7(3)	200.2(1)	26(2)	0.54(5)	0.82(7)	$E1$	7^{-a}	6^+
	334.2(1)	83(4)	0.98(5)		$E2$	7^-	5^-
	362.8(1)	37(3)	0.53(5)		$E1$	7^-	6^+
	1083.6(2)	490(20)	0.60(3)		$E1$	7^-	6^+
	2843.0(1)	18(2)	0.86(7)		$E3$	7^-	4^+
5449.2(5)	2944.4(7)	3(1)			$E2$	6^+	4^+
5662.7(3)	514.4(2)	6(1)			$E2/M1$	7^{+a}	6^+
	677.7(2)	54(4)	0.84(4)		$E2/M1$	7^+	6^+
	1255.1(3)	12(1)			$E2$	7^+	5^+
	1397.7(2)	37(3)	0.56(4)		$E2/M1$	7^+	6^+
	1498.0(4)	2(1)			$E2$	7^+	5^+
5901.6(7)	1637.0(1)	5(1)			$E1$	6^-	6^+
	1736.0(1)	13(1)			$E1$	6^-	5^+
6112.2(4)	963.7(3)	28(2)	0.78(6)	1.07(8)	$E2/M1$	7^+	6^+
	1847.2(5)	17(2)			$E2/M1$	7^+	6^+
	1946.6(5)	8(1)			$E2$	7^+	5^+
6278.4(8)	1042.0(1)	2(1)			($E1$)	(6^-)	$5^{(+)}$
	1264.0(1)	3(1)			($E2/M1$)	(6^-)	5^-
6461.0(3)	348.7(2)	7(2)		0.74(10)	$E2/M1$	8^{+a}	7^+
	798.1(2)	77(4)	0.98(6)	1.16(6)	$E2/M1$	8^+	7^+
	1312.4(4)	21(2)		1.37(10)	$E2$	8^+	6^+
	1475.0(4)	12(1)	0.89(17)		$E2$	8^+	6^+
	2195.9(5)	5(1)	0.93(4)		$E2$	8^+	6^+
6763.0(4)	861.4(4)	3(1)			($E1$)	$7^{(+)}$	6^-
	1525.0(1)	3(1)			$E2$	$7^{(+)}$	$5^{(+)}$
	2498.5(6)	10(1)	0.63(11)		$\Delta I = 1$	$7^{(+)}$	6^+
6810.5(6)	1462.3(4)	391(17)		1.66(8)	$E2$	9^{-a}	7^-
6836.9(4)	1487.8(4)	82(5)	1.63(8)	2.15(10)	$E2/M1$	8^-	7^-
7027.5(3)	914.8(3)	7(1)		1.05(21)	$E2/M1$	8^+	7^+
	1365.0(2)	10(1)		1.11(9)	$E2/M1$	8^+	7^+
	1578.6(4)	6(1)			$E2$	8^+	6^+
	1880.9(5)	10(2)		1.18(12)	$E2$	8^+	6^+
	2041.9(5)	4(2)	0.81(17)		$E2$	8^+	6^+
7249.4(7)	2986.5(7)	16(1)	0.94(10)		$E2$	8^+	6^+
7360.9(16)	2012.2(5)	1(1)			($E2/M1$)	(8)	7^-
7379.8(7)	3114.7(7)	10(1)	0.94(17)		$E2$	8^+	6^+
7433.2(3)	405.7(2)	5(1)			$E2/M1$	9^{+a}	8^+
	972.3(2)	50(5)		1.05(6)	$E2/M1$	9^+	8^+
	1321.1(4)	16(4)			$E2$	9^+	7^+
	1770.6(5)	2(1)			$E2$	9^+	7^+
7465.5(5)	2451.5(6)	1(1)			$E2$	(7^-)	5^-
7530.9(6)	1418.9(4)	3(1)			$E2/M1$	8^+	7^+
	3266.9(8)	4(1)	1.25(23)		$E2$	8^+	6^+
7691.2(4)	928.2(1)	5(1)			($E1$)	8^{-a}	$7^{(+)}$
	1413.9(4)	3(1)			($E2$)	8^-	(6^-)
	1790.2(5)	5(1)		1.40(8)	$E2$	8^-	6^-
7732.3(6)	2586.2(6)	3(1)			$E2$	8^+	6^+
	3465.8(8)	4(1)	1.01(32)		$E2$	8^+	6^+
7760.2(4)	294.7(2)	2(1)			($E2/M1$)	8^-	(7^-)
	948.5(3)	2(1)			$E2/M1$	8^-	9^-

TABLE I. (Continued.)

E_x [keV]	E_γ [keV]	I_{rel}	$R_{Dco}(30 - 83)$		Multipole assignment	I_i^π [\hbar]	I_f^π [\hbar]
			Gate $E2$	Gate $\Delta I = 1$			
	1648.0(4)	4(1)			$E1$	8^-	7^+
	1860.4(5)	1(1)			$E2$	8^-	6^-
	2411.4(6)	10(1)		1.30(10)	$E2/M1$	8^-	7^-
7980.5(4)	547.2(4)	1(1)			$\Delta I = 0$	9^+	9^+
	1519.9(4)	14(5)	0.76(13)		$E2/M1$	9^+	8^+
	2317.5(3)	10(3)	1.32(29)	1.84(33)	$E2$	9^+	7^+
8044.1(3)	283.9(2)	13(2)		0.89(6)	$E2/M1$	9^-	8^-
	352.9(2)	21(3)		0.93(5)	$E2/M1$	9^-	8^-
	683.3(2)	1(1)			($\Delta I = 1$)	9^-	(8)
	1207.0(3)	48(5)	1.08(9)	1.70(8)	$E2/M1$	9^-	8^-
	1233.0(3)	11(2)		1.15(16)	$\Delta I = 0$	9^-	9^-
	1583.3(4)	6(1)		1.09(14)	$E1$	9^-	8^+
	2696.1(6)	29(2)	1.03(4)	1.70(9)	$E2$	9^-	7^-
8073.8(6)	3807.8(9)	1(1)			$E2$	8^+	6^+
8271.9(4)	1435.0(4)	8(1)		1.56(36)	$E2$	10^-	8^-
	1461.6(4)	45(7)			$E2/M1$	10^-	9^-
8389.7(6)	3039.2(7)	8(1)			$E2$	9^-	7^-
8426.6(7)	3077.8(1)	9(1)	1.31(28)	2.3(4)	$E2$	9^-	7^-
8485.3(4)	1648.2(4)	6(1)		0.94(11)	$E2/M1$	9^-	8^-
	1674.5(4)	2(1)			$\Delta I = 0$	9^-	9^-
	3136.9(7)	7(1)	0.95(30)	1.30(19)	$E2$	9^-	7^-
8520.5(4)	249.0(1)	4(1)		1.05(12)	$\Delta I = 0$	10^-	10^-
	476.7(2)	173(5)	0.48(7)	1.03(4)	$E2/M1$	10^-	9^-
	1710.1(4)	104(6)	1.07(5)	1.75(7)	$E2/M1$	10^-	9^-
8688.8(4)	1255.4(4)	17(3)		0.93(7)	$E2/M1$	10^+	9^+
	1661.9(4)	6(1)			$E2$	10^+	8^+
	2227.2(5)	8(2)			$E2$	10^+	8^+
9122.8(4)	601.6(2)	2(1)			$\Delta I = 0$	10^-	10^-
	637.5(2)	18(1)		0.93(11)	$E2/M1$	10^-	9^-
	2311.8(6)	5(1)	0.88(12)	1.05(16)	$E2/M1$	10^-	9^-
9132.2(4)	611.5(2)	251(8)	0.61(3)	1.06(5)	$E2/M1$	11^-	10^-
	1088.2(3)	7(1)			$E2$	11^-	9^-
9264.2(5)	874.1(3)	1(1)			$E2$	11^-	9^-
	2452.2(6)	11(1)	1.20(17)		$E2$	11^-	9^-
9426.1(6)	1992.9(5)	3(1)		1.12(13)	$E2/M1$	10^+	9^+
9622.1(11)	2785.2(7)	3(1)		1.80(34)	$E2$	10^-	8^-
9665.0(4)	1590.9(4)	5(1)	0.98(10)		$E2$	10^+	8^+
	1934.0(5)	4(1)	0.98(17)		$E2$	10^+	8^+
	2134.4(5)	4(1)	1.13(30)		$E2$	10^+	8^+
	2233.0(5)	3(1)	0.54(8)		$E2/M1$	10^+	9^+
	2284.9(6)	3(1)	1.19(20)		$E2$	10^+	8^+
	2416.3(6)	7(1)	0.93(10)		$E2$	10^+	8^+
	2854.4(7)	15(2)	0.49(4)		$E1$	10^+	9^-
	3204.6(7)	2(1)			$E2$	10^+	8^+
9714.6(6)	1287.9(4)	2(1)			($E1$)	(10^+)	9^-
9717.5(6)	454.0(2)	1(1)			$\Delta I = 0$	11^-	11^-
	1196.8(3)	11(1)		1.18(16)	$E2/M1$	11^-	10^-
	1447.1(4)	7(1)			$E2/M1$	11^-	10^-
	2905.9(7)	17(1)	0.88(11)		$E2$	11^-	9^-
9759.8(5)	1239.0(3)	10(1)		0.88(12)	$E2/M1$	11^-	10^-
	2948.8(7)	23(2)	1.09(12)		$E2$	11^-	9^-
9887.7(6)	2638.4(6)	2(1)			$E2$	10^+	8^+
	3079.0(7)	2(1)			$E1$	$10^{(+)}$	9^-
9960.0(4)	827.8(6)	2(1)			$\Delta I = 0$	11^-	11^-
	836.4(3)	13(1)		1.10(5)	$E2/M1$	11^-	10^-

TABLE I. (*Continued.*)

E_x [keV]	E_γ [keV]	I_{rel}	$R_{DCO}(30 - 83)$		Multipole assignment	I_i^π [\hbar]	I_f^π [\hbar]
			Gate $E2$	Gate $\Delta I = 1$			
	1438.6(4)	5(1)			$E2/M1$	11^-	10^-
9989.3(4)	856.9(3)	120(6)	0.65(4)	1.07(5)	$E2/M1$	12^-	11^-
	1468.3(4)	5(1)			$E2$	12^-	10^-
10054.3(8)	789.4(3)	1(1)			($\Delta I = 0$)	(11^-)	11^-
	3243.4(7)	3(1)			($E2$)	(11^-)	9^-
10158.9(11)	894.1(3)	3(1)			($E2/M1$)	(12^-)	11^-
10241.6(7)	3428.9(8)	5(1)			($E2$)	(11^-)	9^-
10696.5(6)	936.7(3)	4(1)	0.62(12)		$E2/M1$	12^-	11^-
	979.1(3)	3(1)	0.48(11)		$E2/M1$	12^-	11^-
10788.6(5)	734.1(2)	2(1)			$E2/M1$	12^-	(11^-)
	828.5(3)	5(1)		0.99(4)	$E2/M1$	12^-	11^-
	1028.0(9)	4(1)			$E2/M1$	12^-	11^-
	1657.5(4)	3(1)			$E2/M1$	12^-	11^-
10825.0(4)	1398.8(9)	1(1)			$E2/M1$	11^+	10^+
	2135.8(5)	3(1)			$E2/M1$	11^+	10^+
	2844.8(7)	3(1)		1.35(16)	$E2$	11^+	9^+
	3390.8(8)	1(1)			$E2$	11^+	9^+
10872.8(6)	1446.6(4)	1(1)			$E2/M1$	11^+	10^+
	2184.4(5)	2(1)			$E2/M1$	11^+	10^+
	2891.7(7)	2(1)			$E2$	11^+	9^+
	3439.2(8)	3(1)			$E2$	11^+	9^+
10977.0(4)	2289.1(6)	<1			$E2/M1$	11^+	10^+
	2705.8(6)	1(1)			$E1$	11^+	10^-
	2996.6(7)	6(3)	1.08(49)	1.90(22)	$E2$	11^+	9^+
	3544.2(8)	5(1)			$E2$	11^+	9^+
11030.4(4)	2341.7(6)	2(1)			$E2/M1$	11^+	10^+
	3048.4(7)	1(1)			$E2$	11^+	9^+
	3596.7(8)	1(1)			$E2$	11^+	9^+
11043.6(5)	1156.8(3)	8(1)	1.01(17)		$E2$	12^+	$10^{(+)}$
	1283.0(4)	2(1)			$E1$	12^+	11^-
	1329.0(4)	1(1)			($E2$)	12^+	(10^+)
	1378.7(4)	69(2)	1.05(6)		$E2$	12^+	10^+
	1911.4(5)	2(1)		1.10(12)	$E1$	12^+	11^-
11078.8(6)	837.1(3)	2(1)			($E2/M1$)	(12^-)	(11^-)
	1025.1(3)	2(1)			($E2/M1$)	(12^-)	(11^-)
11112.8(5)	954.1(3)	1(1)			($E2/M1$)	13^-	(12^-)
	1123.4(3)	58(4)	0.59(4)	1.10(5)	$E2/M1$	13^-	12^-
	1981.1(5)	4(1)		1.48(16)	$E2$	13^-	11^-
11120.2(13)	1498.1(4)	2(1)	0.95(4)		$E2$	12^-	10^-
11224.8(5)	2705(2)	1(1)			($E1$)	(11^+)	10^-
	3792.5(9)	2(1)			($E2$)	(11^+)	9^+
11255.0(4)	224.6(1)	3(1)		0.96(16)	$E2/M1$	12^+	11^+
	278.0(2)	21(1)	0.90(11)	0.90(4)	$E2/M1$	12^+	11^+
	382.8(2)	7(1)		0.88(8)	$E2/M1$	12^+	11^+
	429.9(2)	9(1)		0.92(7)	$E2/M1$	12^+	11^+
	1293.4(4)	6(1)		0.88(10)	$E1$	12^+	11^-
	1590.3(4)	7(1)		2.45(36)	$E2$	12^+	10^+
	2123.4(5)	10(1)		0.78(7)	$E1$	12^+	11^-
11442.7(6)	654.9(2)	4(1)	0.63(12)		$E2/M1$	13^-	12^-
	1683.2(4)	14(1)	0.98(14)		$E2$	13^-	11^-
	1724.9(4)	11(1)	0.99(17)		$E2$	13^-	11^-
11493.3(11)	2361.4(9)	1(1)			($E1$)	(12^+)	11^-
11552.8(7)	764.2(3)	5(1)		0.96(4)	$E2/M1$	13^-	12^-
11785.5(6)	560.8(2)	2(1)		0.94(11)	$E2/M1$	(12^+)	(11^+)
	2654.2(6)	4(1)			($E1$)	(12^+)	11^-

TABLE I. (Continued.)

E_x [keV]	E_y [keV]	I_{rel}	$R_{\text{DCo}}(30 - 83)$		Multipole assignment	I_i^π [\hbar]	I_j^π [\hbar]
			Gate $E2$	Gate $\Delta I = 1$			
11851.2(4)	596.0(2)	66(3)	0.75(8)	1.04(4)	$E2/M1$	13 ⁺	12 ⁺
	872.6(3)	3(1)			$E2$	13 ⁺	11 ⁺
	1862.9(5)	3(1)			$E1$	13 ⁺	12 ⁻
11877.8(7)	1180.7(3)	3(1)	0.57(5)	0.98(7)	($\Delta I = 1$)	(13)	12 ⁻
12273.8(8)	1160.8(3)	26(3)			$E2/M1$	14 ⁻	13 ⁻
	2284.6(6)	4(1)			$E2$	14 ⁻	12 ⁻
12486.1(6)	700.8(2)	4(1)	0.83(9)	0.83(9)	$E2/M1$	(13 ⁺)	(12 ⁺)
	2495.3(6)	3(1)			($E1$)	(13 ⁺)	12 ⁻
12578.4(5)	727.1(2)	47(3)	0.64(12)	1.00(4)	$E2/M1$	14 ⁺	13 ⁺
	1025.1(3)	2(1)			$E1$	14 ⁺	13 ⁻
	1323.9(4)	3(1)			$E2$	14 ⁺	12 ⁺
12741.9(7)	1956.0(12)	2(1)			$E1$	13 ⁺	12 ⁻
	2753.2(7)	1(1)			$E1$	13 ⁺	12 ⁻
12774.5(6)	1281.1(4)	1(1)	1.21(6)		($E2$)	14 ⁺	(12 ⁺)
	1730.4(4)	113(6)			$E2$	14 ⁺	12 ⁺
12859.1(8)						13 ⁺	
13037.1(15)	1916.9(5)	4(1)	1.10(5)		$E2$	14 ⁻	12 ⁻
13245.7(8)	2202.3(5)	2(1)	0.63(12)		$E2/M1$	13 ⁺	12 ⁺
	2456.4(6)	2(1)			$E1$	13 ⁺	12 ⁻
13281.6(9)	1839.1(5)	5(1)			($E1$)	(14 ⁺)	13 ⁻
	2238.1(9)	2(1)			($E2$)	(14 ⁺)	12 ⁺
13353.0(7)	866.8(3)	6(1)		1.13(12)	$E2/M1$	(14 ⁺)	(13 ⁺)
13615.2(7)	2172.9(5)	15(1)	1.05(25)		$E2$	15 ⁻	13 ⁻
	2061.2(5)	2(1)			$E2$	15 ⁻	13 ⁻
13662.3(5)	1083.9(3)	36(3)		1.60(22)	$E2/M1$	15 ⁺	14 ⁺
	1811.0(5)	4(1)			$E2$	15 ⁺	13 ⁺
13810.0(9)	1536.2(4)	3(1)		0.97(12)	($E2/M1$)	(15 ⁻)	14 ⁻
	2697.2(6)	2(1)			($E2$)	(15 ⁻)	13 ⁻
14201.0(8)	848.0(3)	3(1)			$E2/M1$	(15 ⁺)	(14 ⁺)
14462.8(7)	1217.1(3)	9(2)	0.96(8)		$E2$	15 ⁺	13 ⁺
	1604.3(4)	6(1)	0.90(14)		$E2$	15 ⁺	13 ⁺
	1688.8(4)	8(1)	0.45(4)		$E2/M1$	15 ⁺	14 ⁺
	1722.0(4)	16(1)	1.02(11)		$E2$	15 ⁺	13 ⁺
	2189.9(5)	2(1)			$E1$	15 ⁺	14 ⁻
14644.5(9)	1870.8(5)	55(5)	0.98(6)		$E2$	16 ⁺	14 ⁺
14803.0(7)	1141.1(3)	14(1)		0.89(9)	$E2/M1$	16 ⁺	15 ⁺
	2224.5(5)	4(1)			$E2$	16 ⁺	14 ⁺
14933.6(8)	1651.7(4)	4(1)	1.02(8)		($E2$)	16 ⁺	(14 ⁺)
	2158.9(5)	15(2)			$E2$	16 ⁺	14 ⁺
15164.6(9)	963.8(3)	2(1)			($E2/M1$)	(16 ⁺)	(15 ⁺)
15281.0(16)	2243.9(5)	3(1)			($E2$)	(16 ⁻)	14 ⁻
16026.4(7)	1381.2(4)	2(1)	1.13(10)		$E2/M1$	17 ⁺	16 ⁺
	1562.9(4)	64(3)			$E2$	17 ⁺	15 ⁺
16097.8(16)	1294.8(1)	1(1)			($E2/M1$)	(17 ⁺)	16 ⁺
16194.1(11)	2578.9(6)	6(1)	1.05(17)		$E2$	17 ⁻	15 ⁻
16241.6(18)	1077(1)	1(1)			($E2/M1$)	(17 ⁺)	(16 ⁺)
16841.9(10)	2196.9(5)	23(3)	0.87(7)		$E2$	18 ⁺	16 ⁺
17235.6(11)	2301.9(6)	6(1)	1.16(13)		$E2$	18 ⁺	16 ⁺
17911.3(10)	1884.9(5)	42(3)	1.13(10)		$E2$	19 ⁺	17 ⁺
18130.9(19)	2849.9(7)	2(1)			($E2$)	(18 ⁺)	(16 ⁺)
19238.0(15)	3043.9(7)	1(1)			($E2$)	(19 ⁻)	17 ⁻
19504.0(14)	2661.9(6)	5(1)	1.05(13)		$E2$	20 ⁺	18 ⁺
20017.6(15)	2782.0(7)	2(1)			($E2$)	(20 ⁺)	18 ⁺
20177.8(13)	2265.9(6)	10(1)	1.21(14)		$E2$	21 ⁺	19 ⁺
22862.8(19)	3359.0(8)	1(1)			($E2$)	(22 ⁺)	20 ⁺
22996.1(17)	2818.9(7)	2(1)	0.95(15)		$E2$	23 ⁺	21 ⁺

^aAssignment supported by or based on the evaluation of Ref. [38].

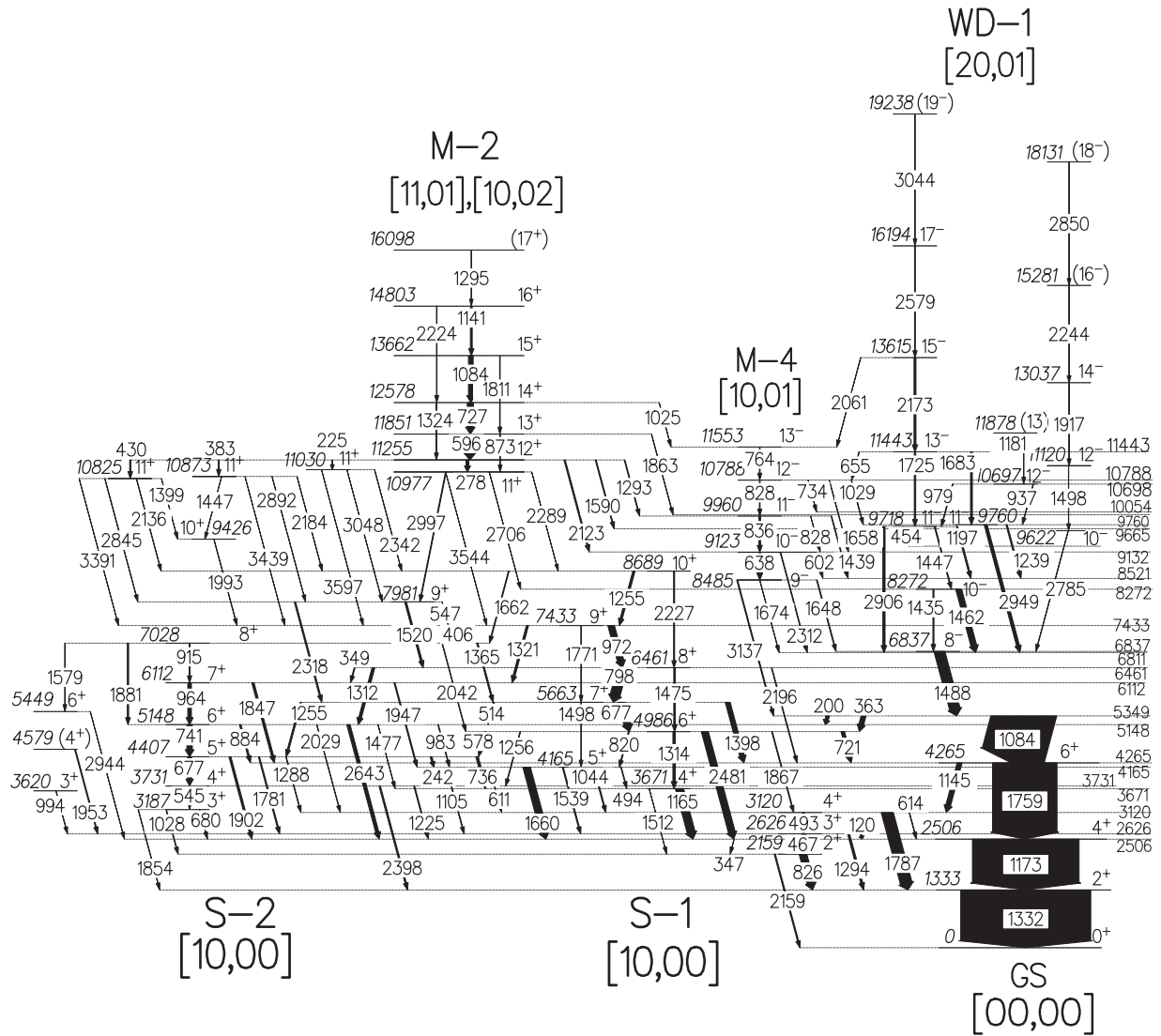


FIG. 1. Proposed high-spin level scheme of ^{60}Ni . The energies of the transitions are labeled in keV and the widths of the arrows are proportional to the relative intensities of the γ -ray transitions. Tentative transitions are represented with a dashed arrow. The structures are labeled with both a short-hand notation and the proposed Cranked Nilsson-Strutinsky configurations. See Sec. IV B for details.

The Ge detectors in GAMMASPHERE were grouped in three ‘pseudo’-rings labeled ‘30’ (Ge detectors at $\theta = 31.7^\circ, 37.4^\circ, 142.6^\circ, 148.3^\circ,$ and 162.7°), ‘53’ (Ge detectors at $\theta = 50.1^\circ, 58.3^\circ, 121.7^\circ,$ and 129.9°), and ‘83’ (Ge detectors at $\theta = 79.2^\circ, 80.7^\circ, 90.0^\circ, 99.3^\circ,$ and 100.8°), respectively. This procedure was found to provide a good compromise between statistics and significance. The three experiments were combined to construct the DCO matrices, labeled (30–83), (53–83), and (30–53). Average DCO ratios were obtained after correcting the intensities by the efficiency of each experiment and including the attenuation of the angular correlation due to the finite size of the detectors. The statistical evaporation of the four protons and the in essence close to 4π (in the center of mass system) geometry of the charged-particle detector arrays do not affect the DCO-ratios/ γ -ray angular correlations beyond the typical systematic and statistical uncertainties. A more comprehensive study of the effects

of charged-particle emission and detection on γ -ray angular correlations is presently being performed [34]. No significant deviations between the final average DCO ratio and the individual DCO values corrected for any of the experiments were found using this technique. For example, the DCO-ratio $R_{\text{DCO}}(30-83)$ is defined as [35]

$$R_{\text{DCO}}(30-83) = \frac{I(\gamma_1 \text{ at } 30^\circ; \text{ gated with } \gamma_2 \text{ at } 83^\circ)}{I(\gamma_1 \text{ at } 83^\circ; \text{ gated with } \gamma_2 \text{ at } 30^\circ)}, \quad (1)$$

where the intensities I were extracted from a $4p$ - and TE-gated γ - γ matrix with γ rays detected at 30° sorted on one axis and 83° on the other axis of the matrix. The ratios $R_{\text{DCO}}(30-53)$ and $R_{\text{DCO}}(53-83)$ are defined and determined accordingly. The $R_{\text{DCO}}(30-83)$ values, which could be deduced for most of the γ -ray transitions in the level scheme, are summarized in Table I. They were obtained by gating on known stretched

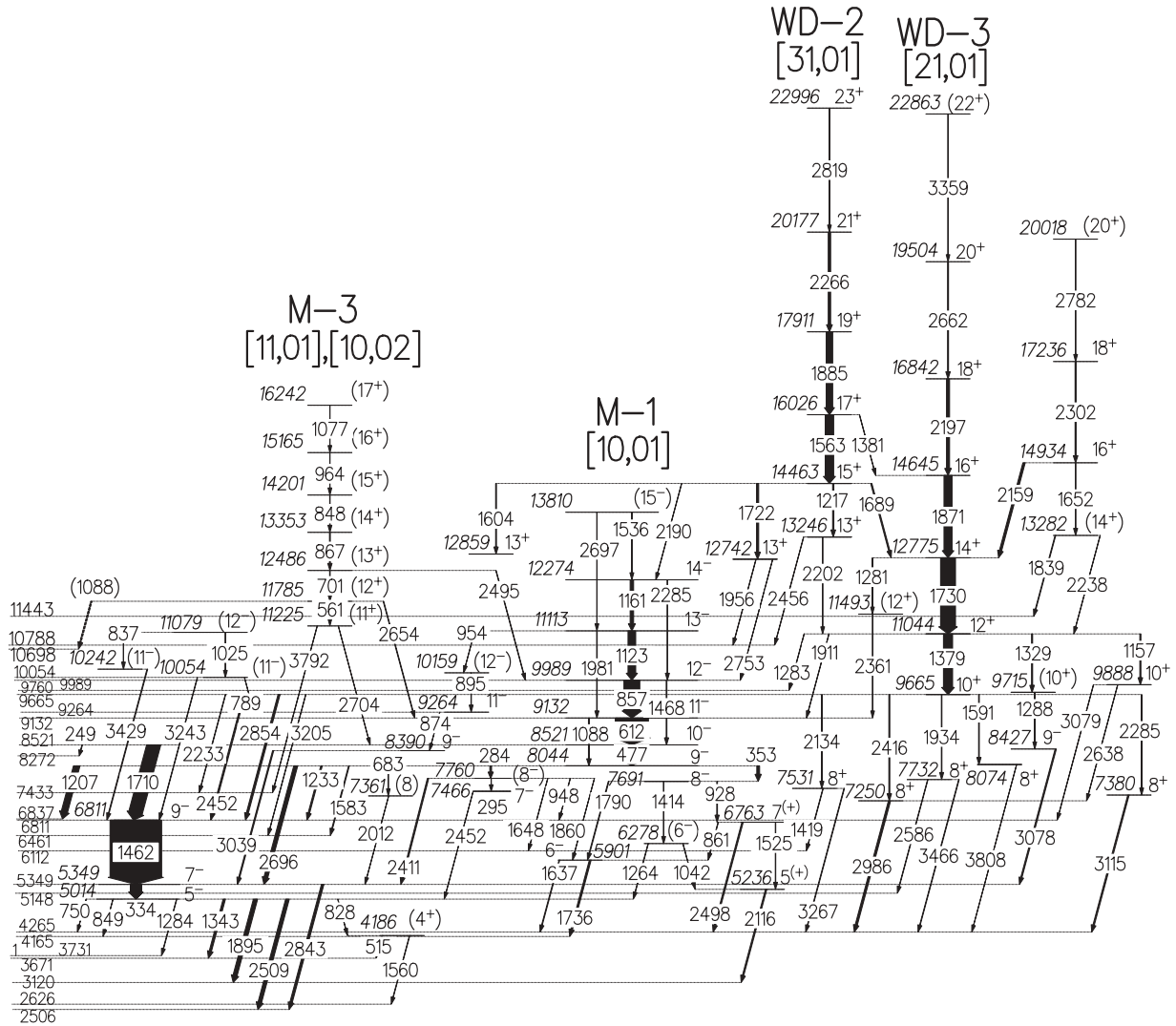


FIG. 1. (Continued.)

quadrupole electric ($E2$) and $\Delta I = 1$ transitions, where the following statements apply:

If gating on (γ_2) a stretched $\Delta I = 2$ transition

$$R_{\text{DCO}} \left\{ \begin{array}{l} = 1.0 \quad \text{if } \gamma_1 \text{ is a } E2 \text{ transition} \\ \approx 1.0 \quad \text{if } \gamma_1 \text{ is a } \Delta I = 0 \text{ transition} \\ \approx 0.6 \quad \text{if } \gamma_1 \text{ is a } \Delta I = 1 \text{ transition} \end{array} \right\}. \quad (2)$$

If gating on (γ_2) a stretched and pure $\Delta I = 1$ transition

$$R_{\text{DCO}} \left\{ \begin{array}{l} = 1.0 \quad \text{if } \gamma_1 \text{ is a } \Delta I = 1 \text{ transition} \\ \leq 1.7 \quad \text{if } \gamma_1 \text{ is an } E2 \text{ or a } \Delta I = 0 \text{ transition} \end{array} \right\}. \quad (3)$$

Deviations from the latter may arise from quadrupole admixtures, i.e., nonzero $\delta(E2/M1)$ mixing ratios ($M2$ admixtures into $E1$ dipoles are considered unlikely). In the discussion below we will refer to the DCO ratio obtained with a gate in an $E2$ -transition as $R_{\text{DCO-}E2}$, and $R_{\text{DCO-}\Delta I}$ correspondingly for DCO ratios from $\Delta I = 1$ transitions.

The investigation of the DCO ratios obtained with the three possible different angle combinations for a given transition allowed an evaluation of $\delta(E2/M1)$ mixing ratios for some of the $\Delta I = 0$ and stretched $\Delta I = 1$ transitions. The results are given in Table II together with the respective $R_{\text{DCO}(30-53)}$, $R_{\text{DCO}(30-83)}$, and $R_{\text{DCO}(53-83)}$ ratios. The phase convention of Rose and Brink [36] is used for the mixing ratios. The alignment coefficients α_2 were fixed using the relation [37]

$$\alpha_2 = 0.60 + 0.02 \cdot E_x \text{ [MeV]}, \quad \Delta\alpha_2 = \pm 0.05. \quad (4)$$

As an example, Fig. 2 provides the analysis of the 1294-keV $3^+ \rightarrow 2^+$ transition. The weighted mean of the three consistent solutions for the mixing ratio, $\delta(E2/M1) = -0.11(15)$ is given in Table II. All the reported mixing ratios are consistent for all three angle combinations.

The lifetimes of the states at the top of the rotational bands in the mass $A \approx 60$ region are in the femtosecond regime. Therefore, they are likely to decay while the ^{60}Ni nuclei are slowing down in the thin target foil. The Doppler

TABLE II. DCO ratios of three different angle combinations and deduced $\delta(E2/M1)$ mixing ratios for a number of $\Delta I = 0$ and stretched $\Delta I = 1$ transitions. See text for details.

E_x [keV]	E_γ [keV]	Gate	R_{DCO}			α_2	δ
			30–53	30–83	53–83		
Structure GS							
2158.9(2)	826.1(2)	1173	1.04(8)	1.07(8)	1.00(6)	0.64(5)	0.2(2)
2626.1(2)	467.1(1)	1173	1.09(8)	1.02(8)	1.02(7)	0.65(5)	$-15 < \delta < -3$, $-0.38(18)$
	1293.7(2)	1173	0.73(3)	0.56(2)	0.74(3)	0.65(5)	$-0.11(15)$
3119.5(2)	493.4(1)	467	0.88(4)	0.99(4)	1.43(6)	0.66(5)	$-0.65 < \delta < 0.14$
Structure S-1							
3671.2(2)	1165.2(2)	1173	1.02(4)	0.95(4)	0.97(4)	0.67(5)	$+0.10(8)$, $-1.4(5)$
4165.6(2)	1659.6(3)	1173	0.44(5)	0.32(3)	0.54(4)	0.68(5)	$0.3 < \delta < 2.0$
5662.7(3)	677.7(2)	2481	0.83(4)	0.84(4)	0.85(4)	0.71(5)	$-0.35 < \delta < -0.02$
	1397.7(2)	1759	0.65(5)	0.56(4)	0.63(5)	0.71(5)	0.12(13)
6461.0(3)	798.1(2)	1759	1.08(5)	0.98(6)	1.03(5)	0.73(5)	$-0.45(5)$
7433.2(3)	972.3(2)	1759	0.99(8)	1.07(8)	0.94(10)	0.75(5)	$-0.4(2)$
8688.8(4)	1255.4(4)	1759	0.89(7)	1.06(9)	1.07(8)	0.77(5)	$-0.5(3)$
Structure S-2							
5148.4(3)	740.9(2)	1173	1.05(7)	0.81(6)	1.03(7)	0.70(5)	$-0.4(1)$
6112.2(4)	963.7(3)	1173	0.88(6)	0.78(6)	0.95(6)	0.72(5)	$-0.3(2)$
Structure M-1							
8044.1(3)	1207.0(3)	612	1.33(5)	1.70(8)	1.30(5)	0.76(5)	$-0.37(4)$
8520.5(4)	476.7(2)	612	1.03(4)	0.98(4)	1.07(5)	0.77(5)	0.00(5)
	1710.1(4)	612	1.75(7)	1.33(6)	1.25(5)	0.77(5)	$-0.34(5)$
9132.2(4)	611.5(2)	1462	0.77(4)	0.61(3)	0.80(4)	0.78(5)	$-0.08(7)$
9989.3(4)	856.9(3)	1462	0.85(5)	0.65(4)	0.81(4)	0.80(5)	$-0.13(15)$
11112.8(5)	1123.4(3)	1462	0.91(6)	0.59(4)	0.79(5)	0.82(5)	$-0.13(7)$
12273.8(8)	1160.8(3)	1462	0.87(6)	0.57(5)	0.77(5)	0.84(5)	$-0.11(6)$
Structure M-2							
11255.0(4)	224.6(1)	727	0.77(11)	0.96(16)	0.92(11)	0.82(5)	0.12(10)
	278.0(2)	727	0.89(5)	0.90(4)	1.02(5)	0.82(5)	0.03(5)
	382.8(2)	727	0.95(8)	0.88(8)	0.98(7)	0.82(5)	0.05(4)
	429.9(2)	727	0.89(7)	0.92(7)	1.03(7)	0.82(5)	0.04(4)
11851.2(4)	596.0(2)	727	0.97(5)	1.04(4)	1.03(5)	0.84(5)	0.03(4)
12578.4(5)	727.1(2)	727	1.05(6)	1.00(4)	1.04(5)	0.85(5)	$-0.03(5)$
14803.0(7)	1141.1(3)	727	0.92(12)	0.89(9)	1.08(7)	0.89(5)	0.01(10)
Structure WD-2							
14462.8(7)	1688.8(4)	1730	1.01(4)	0.45(4)	0.61(7)	0.89(5)	0.0(2)

correction of the γ -ray transitions is performed using the velocity of the recoils *after* the target, such that the peaks of transitions below 13 MeV excitation energy are lined up in the Ge-detector spectra taken at different detector angles. Thus the γ -rays emitted during the slowing down process in the target have additional Doppler shifts, particularly in spectra of Ge detectors at forward and backward angles. This effect has been corrected with an additional Doppler-shift correction

$$E_\gamma = \frac{E'_\gamma}{1 + F\beta \cos(\theta)} + 0.5, \quad (5)$$

for the γ -rays emitted from states in the well-deformed structures with excitation energies higher than 7 MeV, structures WD-1, WD-2, and WD-3 (see Fig. 1). In Eq. (5), $E'_\gamma(E_\gamma)$ is the corrected (uncorrected) γ -ray energy in keV, θ is the detector angle, $\beta = v/c$ the residual nucleus velocity outside the target,

and F is the term that gives the modification to the velocity in this new Doppler correction. For the $A \approx 60$ mass region an average parametrization for γ rays emitted from the deformed structures under the conditions $1.5 < E'_\gamma(\text{MeV}) < 3.5$ of $F = -2.0 \times 10^{-8}(E'_\gamma)^2 + 1.3 \times 10^{-4}(E'_\gamma) - 0.14$, with E'_γ in keV, has been used. For $E_\gamma > 3.5$ MeV a constant F value has been used.

III. RESULTS

The level scheme of Fig. 1 has a degree of complexity. However, groups of transitions (and states) can be isolated as single structures that connect to each other by other transitions. These groups have apparent definite structural characteristics. Generally speaking we can classify them as: magnetic bands

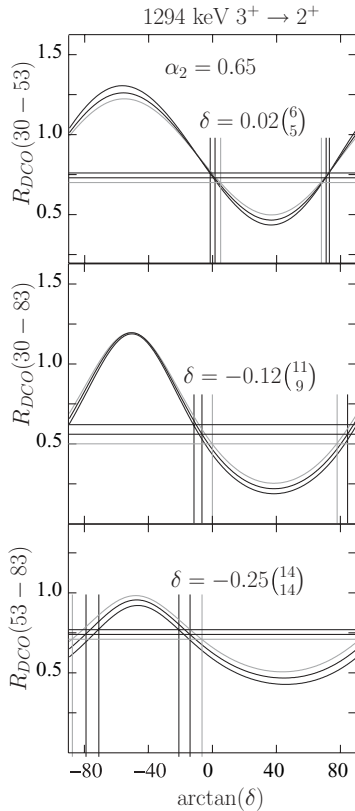


FIG. 2. Analysis of the DCO ratios of the 1294-keV $3^+ \rightarrow 2^+$ transition using three different detector angle combinations. The experimental DCO ratio is represented by the horizontal lines. The DCO ratios calculated as a function of the multipole mixing ratio $\delta(E2/M1)$ for the given alignment (including uncertainties) are shown by the three curves in each panel. The crossing of the curves with the experimental DCO-ratios mark possible solutions for the mixing ratio, indicated by the vertical lines.

(M-1, M-2, M-3, and M-4), well deformed states (WD-1, WD-2, and WD-3), and single-particle states (GS, S-1, and S-2). Each one of the analyzed structures has been labeled in Fig. 1 with a name and the particle configurations using a convention that will be explained in Sec. IV. Except for the band M-3, all the excited rotational bands are connected to the low-spin states by a collection of linking transitions for which DCO measurements were possible. This fact allowed firm spin and parity assignment to the lowest states in the bands. DCO ratios and spin assignments are reported in Table I, mixing ratios are listed in Table II, as mentioned in the previous section. The tentative spin and parity assignments in the states near the top of the bands are based in their regular rotational behavior.

A. Structures GS, S-1, and S-2

Structures GS, S-1, and S-2 correspond to low-spin low-lying positive-parity states. They are consistent with previously reported level schemes [20–24] but noticeably extended. The previous spin and parity assignments have been confirmed with a few corrections at high excitation energies. Figure 3 focuses on these structures showing the

γ -ray spectrum in coincidence with the 677-keV doublet transition ($7^+ \rightarrow 6^+$ in S-1, $5^+ \rightarrow 4^+$ in S-2). Figure 4 shows a spectrum in coincidence with the 200-keV, $7^- \rightarrow 6^+$ transition depopulating the state at $E_x = 5349$ keV (in the discussion below E_x will make reference to the excitation energy of the states).

1. Structure GS

The GS structure is composed of the states from 0^+ at $E_x = 0$ keV to 6^+ at $E_x = 4265$ keV, and the states $E_x = 2159$ keV 2^+ , 2626 keV 3^+ , and 3120 keV 4^+ . The positive parity of the structure is consistent with the stretched $E2\gamma$ -ray transition and with the values for the mixing ratios of the $\Delta I = 1$ transitions, and it is in agreement with Refs. [20,22] (see Tables I and II). The 614-keV transition between states at $E_x = 3120$ keV 4^+ and 2506 keV 4^+ is reported for the first time. In Figs. 3 and 4 it is possible to see the highest intensity transitions of the GS structure.

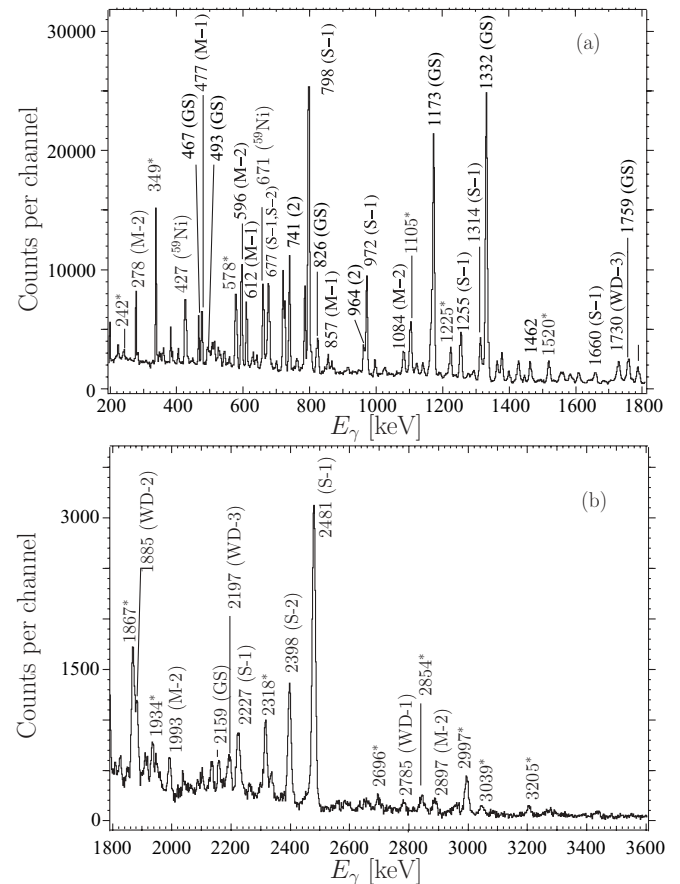


FIG. 3. Spectra in coincidence with the 677-keV doublet transition $7^+ \rightarrow 6^+$ (S-1) and $5^+ \rightarrow 4^+$ (S-2). (a) from 200 keV to 1800 keV, and (b) from 1800 keV to 3600 keV. The transitions in coincidence have been labeled with their energies in keV and in parenthesis the name of the structure to which they belong within the ^{60}Ni level scheme shown in Fig. 1. To facilitate the reading only the most relevant peaks have been labeled. Asterisks correspond to transitions between structures.

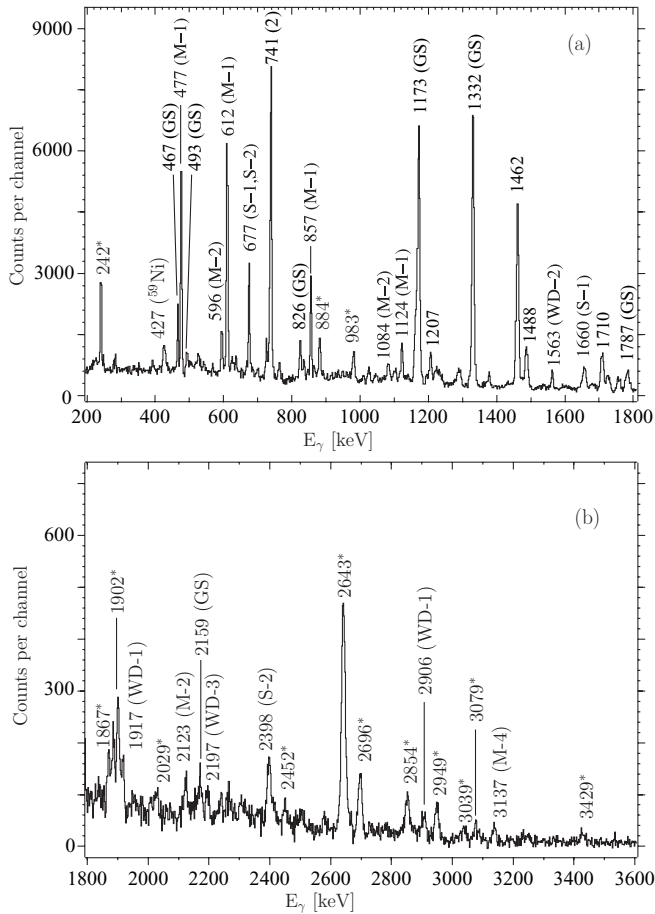


FIG. 4. Spectra in coincidence with the 200-keV $7^- \rightarrow 6^+$ transition (GS \rightarrow S-2). (a) From 200 to 1800 keV. (b) From 1800 to 3600 keV. See caption to Fig. 3 for additional explanations.

2. Structure S-1

Structure S-1 corresponds to states forming a sequence of strong $\Delta I = 1$ transitions from the 4^+ state at $E_x = 3671$ keV to the 10^+ state at $E_x = 8689$ keV. The 5^+ assignment for the state at $E_x = 4165$ keV is confirmed by the low $R_{\text{DCO-E2}}$ value of the 1660-keV, $5^+ \rightarrow 4^+$ transition that depopulates the state and its mixing ratio $0.3 < \delta < 2.0$, indicating a strong $E2/M1$ mixing. The 1165-keV $4^+ \rightarrow 4^+$ transition that depopulates the 4^+ state at $E_x = 3671$ keV has $R_{\text{DCO-E2}} \approx 1.0$, which is in agreement with the $\Delta I = 0$ assignment. Finally, the 2481-keV, $6^+ \rightarrow 4^+$ transition that depopulates the 6^+ level at $E_x = 4986$ keV has $E2$ character due to its $R_{\text{DCO-E2}} \approx 1.0$, confirming the 6^+ assignment and matching with the 4^+ assignment of the level at $E_x = 3671$ keV, since the 1314-keV, $6^+ \rightarrow 4^+$ transition has an $E2$ character deduced as well from $R_{\text{DCO-E2}} \approx 1.0$. The sequence of $\Delta I = 1$ transitions in structure S-1 exhibit an almost constant value in the mixing ratio, $\delta \approx -0.4$, and the R_{DCO} values confirm their $\Delta I = 1$ character. Additionally the weak crossover $E2$ transitions between pairs of states confirm the $\Delta I = 1$ assignment to the set of γ -ray transitions, for example, the 1475-keV transition from the 8^+ state at $E_x = 6461$ to the 6^+ state at $E_x = 4986$ keV matches with the energy difference of the 798-keV, $8^+ \rightarrow 7^+$ and 677-keV, $7^+ \rightarrow 6^+$ transitions

and is in agreement with the assignment of $\Delta I = 1$ for the latter γ -ray transitions.

3. Structure S-2

Structure S-2 is formed by a set of states from the 3187-keV 3^+ state to the 7028-keV 8^+ state. Similar to structure S-1, it has a sequence of strong $\Delta I = 1$ transitions. The $I = 3\hbar$ assignment to the 3^+ state at $E_x = 3187$ keV is justified with $R_{\text{DCO-E2}} = 0.63$ for the 1028-keV $3^+ \rightarrow 4^+$ γ -ray that depopulates the state. This R_{DCO} ratio is consistent with a $\Delta I = 1$ character. The 2398-keV γ -ray that depopulates the 4^+ state at $E_x = 3731$ keV has $R_{\text{DCO-E2}} \approx 1.0$, which is consistent with an $E2$ transition. Additionally, the 545-keV transition from the same state to the 3^+ state at $E_x = 3187$ keV has a $\Delta I = 1$ character that matches with the 4^+ and 3^+ spin and parity assignments to these states. The 677-keV γ -ray transition from the 5^+ state at $E_x = 4407$ keV to the 4^+ state at $E_x = 3731$ keV is a doublet with the 677-keV γ -ray transition from the 5663-keV 7^+ state to 4986-keV 6^+ state in the structure S-1. The sequence of $\Delta I = 1$ transitions from the 5^+ to the 8^+ state is strongly supported by $R_{\text{DCO-E2}} \approx 1.0$, $R_{\text{DCO-E2}} < 1.0$ for the 741-keV $6^+ \rightarrow 5^+$ transition, together with $\delta \approx -0.4$ for both the latter transition and the 964-keV $7^+ \rightarrow 6^+$.

Between structures GS, S-1, and S-2 we observe both new and also previously reported transitions. In general, the new transitions have a relative intensity lower than 10 units (compare to 1000 units the most intense transition), with some exceptions like the 884-keV γ -transition from the $E_x = 5148$ keV, 6^+ state (S-2) to the $E_x = 4265$ keV 6^+ state (GS), and the transition of 1321-keV from the $E_x = 7433$ keV 9^+ state to the $E_x = 6112$ keV 7^+ state (S-1 \rightarrow S-2).

B. Structures M-1, M-2, M-3, and M-4

1. Structure M-1

Structure M-1 has been previously reported up to an excitation energy of 12274 keV [20]. The present analysis has extended it by one transition up to $E_x = 13810$ keV. Figure 5(a) focuses on this structure and clearly shows the $\Delta I = 1$ transitions at 477-keV $10^- \rightarrow 9^-$, 612-keV $11^- \rightarrow 10^-$, 1123-keV $13^- \rightarrow 12^-$, and 1161-keV $14^- \rightarrow 13^-$. The depopulating 2411-keV $8^- \rightarrow 7^-$ transition that connects the M-1 band with the GS structure is also seen. The spin 9^- of the state at $E_x = 8044$ keV is justified by the stretched- $E2$ character of the 2696-keV $9^- \rightarrow 7^-$ transition decaying to the 5349-keV 7^- state. The 1583-keV γ -ray transition from the 9^- state at $E_x = 8044$ keV is consistent with an $E1$ character from its $R_{\text{DCO-E2}} \approx 1.0$, and it is populating the $E_x = 6461$ keV 8^+ state. This is in agreement with the 9^- spin and parity assignment of the $E_x = 8044$ keV state. From the 8044-keV, 9^- state, the decay-out of the structure is formed by a set of transitions connecting the M-1 structure with the single-particle states.

The M-1 structure has an interesting sequence of $\Delta I = 1$ transitions with stretched $M1$ character from the 9^- state

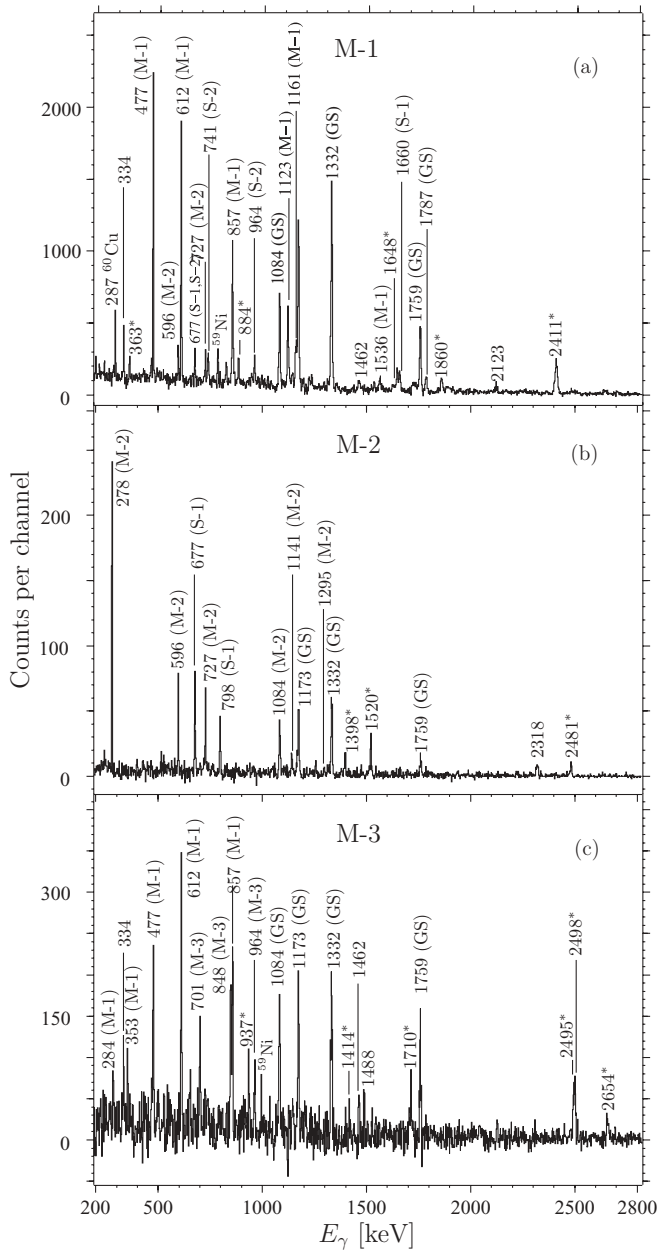


FIG. 5. (a) Spectrum in double coincidence with the 284-keV $9^- \rightarrow 8^-$ transition and one of the 477-keV, 612-keV, or 857-keV transitions in M-1. (b) Spectrum in double coincidence with the 2997-keV $11^+ \rightarrow 9^+$ transition and one of the 596-keV or 727-keV transitions in M-2. (c) Spectrum in double coincidence with the 867-keV ($14^+ \rightarrow 13^+$) transition in M-3 and one of the 477-keV or 612-keV or 857-keV transitions in M-1. See caption to Fig. 3 for additional explanations.

at $E_x = 8044$ keV to the (15^-) state at $E_x = 13810$ keV. This behavior is confirmed by $R_{\text{DCO}} - \Delta I \approx 1.0$ and $\delta \lesssim 0.0$ for the 1161-keV $14^- \rightarrow 13^-$, 1123-keV $13^- \rightarrow 12^-$, 857-keV $12^- \rightarrow 11^-$, 612-keV $11^- \rightarrow 10^-$, and 477-keV $10^- \rightarrow 9^-$ transitions. A set of weak cross-over transitions between pairs of states is observed in the M-1 band. These transitions have a probable stretched $E2$ character and are around ten to thirty times weaker than the $M1$ transitions.

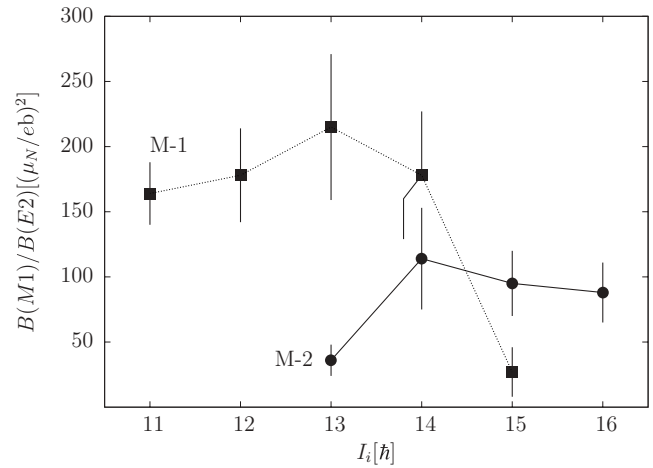


FIG. 6. Experimental $B(M1)/B(E2)$ ratios for the M-1 and M-2 bands. See text for details.

An example of this kind of weak cross-over transition is the 1468-keV $12^- \rightarrow 10^-$ γ -ray from the state at $E_x = 9989$ keV to the state at $E_x = 8521$ keV. These cross-over transitions, reported for the first time here, indicate a low electric quadrupole deformation in the band [18]. In Fig. 6 the experimental $B(M1)/B(E2)$ values for the M-1 and M-2 bands are shown. Even under the assumption of low $B(E2)$ values due to its low quadrupole deformation, this figure suggests large $B(M1)$ values. This kind of magnetic band (structures with a sequence of strong stretched $M1$ transitions with weak cross-over $E2$ transitions between pairs of states) is one of the most interesting experimental results of this work. Similar structures will be described below with the names M-2, M-3, and M-4.

2. Structure M-2

Structure M-2 is composed of states from the 12^+ state at $E_x = 11255$ keV to the (17^+) state at $E_x = 16098$ keV. Figure 5(b) is focused on this structure and shows the strong $\Delta I = 1$ transitions at 278-keV $12^+ \rightarrow 11^+$, 596-keV $13^+ \rightarrow 12^+$, 727-keV $14^+ \rightarrow 13^+$, 1084-keV $15^+ \rightarrow 14^+$, and 1141-keV $16^+ \rightarrow 15^+$. Their stretched $M1$ multipolarity character is confirmed by the $\delta \approx 0.0$ and $R_{\text{DCO}} - \Delta I \approx 1.0$ values. As in the M-1 structure, weak cross-over $E2$ transitions between pairs of states are observed. The assignment of 11^+ to the state at $E_x = 10977$ keV is supported by the stretched $E2$ character of the 2997-keV $11^+ \rightarrow 9^+$ transition that depopulates the state. The 12^+ assignment for the state at $E_x = 11255$ keV is supported by the stretched $M1$ character of the 278-keV $12^+ \rightarrow 11^+$ transition that is populating the 11^+ state at $E_x = 10977$ keV. A set of stretched $M1$ transitions depopulating the 12^+ state at $E_x = 11255$ keV is observed: 225, 383, and 430-keV. Their $M1$ character allows to assign the 11^+ value to the states at $E_x = 11030$ keV, $E_x = 10873$ keV and $E_x = 10825$ keV that they are populating, respectively. The transitions that depopulate these 11^+ states have in general $E_\gamma > 2$ MeV and have too low intensity to perform DCO measurements. Note that the transitions depopulating

the structure M-2 with $E_\gamma > 2.5$ MeV have $E2$ character, similar to the previously explained 2997-keV $11^+ \rightarrow 9^+$ transition, whereas those γ -rays with $E_\gamma < 2.5$ MeV should be mixed $E2/M1$, like the 2289-keV $11^+ \rightarrow 10^+$ transition. The transitions depopulating the $E_x = 10977$ keV 11^+ state are populating the 9^+ and 10^+ states in structure S-1, the only one exception to this is the 2706-keV transition that is populating the 10^- state at $E_x = 8272$ keV. The 1084-keV $15^+ \rightarrow 14^+$ transition in the M-2 structure is a doublet with the very strong transition emitted from the 7^- state at $E_x = 5349$ keV to the 6^+ state at $E_x = 4265$ keV in the structure GS. Nevertheless, the $\gamma\gamma\gamma$ cube analysis allows for a definitive placement and a correct value for the intensity of the 1084-keV $15^+ \rightarrow 14^+$ γ -ray. The placement is additionally supported by the two parallel weak cross-over transitions of 2224-keV from the 16^+ state at $E_x = 14803$ keV to the 14^+ state at $E_x = 12578$ keV and of 1811-keV from the 15^+ state at $E_x = 13662$ keV to the 13^+ state at $E_x = 11851$ keV.

3. Structure M-3

Structure M-3 corresponds to a set of states from (11^+) at $E_x = 11225$ keV to the state (17^+) at $E_x = 16242$ keV. Figure 5(c) shows a coincidence spectrum with the 867-keV ($14^+ \rightarrow 13^+$) transition and any one of the M-1 transitions at 477, 612, or 857-keV. The 2654-keV ($12^+ \rightarrow 11^-$) and the 2495-keV ($13^+ \rightarrow 12^-$) transitions connecting the structures M-3 and M-1 are clearly observed. The intra-structure M-3 transitions 848-keV ($15^+ \rightarrow 14^+$) and 964-keV ($16^+ \rightarrow 15^+$), though weak, can also be observed. The (11^+) state at $E_x = 11225$ keV depopulates by two high-energy γ -rays for which no DCO measurements were possible. Taking the most plausible character and multipolarity assignments, namely $E1$ for the 2704-keV ($11^+ \rightarrow 10^-$) transition populating the M-1 10^- state at $E_x = 8521$ keV, and $E2$ for the 3792-keV ($11^+ \rightarrow 9^+$) transition that populates the S-1 9^+ state at $E_x = 7433$ keV, a tentative (11^+) assignment for the $E_x = 11225$ keV state is proposed. The latter assumption is based on the observed tendency for the transitions with $E_\gamma > 2.0$ MeV to have $E2$ character. Between the (15^+) state at $E_x = 14201$ keV and the (12^+) state at $E_x = 11785$ keV three transitions (848, 867, and 701-keV) with $\Delta I = 1$ are observed, confirmed by the $R_{\text{DCO}} - \Delta I \approx 1.0$. Additionally, in agreement with the $E1$ character tentatively assigned to the 2704-keV ($11^+ \rightarrow 10^-$) transition, the parallel linking transitions at 2654-keV ($12^+ \rightarrow 11^-$) and 2495-keV ($13^+ \rightarrow 12^-$) should have also $E1$ character, justifying spin and parity assignment for the (12^+), (13^+), (14^+), and (15^+) M-3 states. The assignment of (16^+) and (17^+) for the two highest states of the band is proposed based on the apparent regular increase of their excitation energies.

The $I^\pi = 9^-$ assignment to the band head of structure M-4 at $E_x = 8485$ keV is fixed by the stretched $E2$ character of the 3137-keV linking transition connecting with the 7^- state at $E_x = 5349$ keV. The spin and parity assignments to the other four M-4 states from the $E_x = 9123$ keV 10^- state to the $E_x = 11553$ keV 13^- state are based on the $R_{\text{DCO}} - \Delta I \approx 1.0$ of

the intrastructure transitions (638, 836, 282, and 764-keV). The $\Delta I = 1$ character ($R_{\text{DCO}} - \Delta I \approx 1.0$) of the M-4 depopulating 1648-keV $9^- \rightarrow 8^-$ transition fixes $I^\pi = 8^-$ for the state at $E_x = 6837$ keV.

C. Structures WD-1, WD-2, and WD-3

1. Structure WD-1

Structure WD-1 is composed of two rotational bands. The odd-spin structure displays a singular decay since the state at $E_x = 11443$ keV 13^- depopulates through two “twin” branches. The first step of each decay path consists of the 1725-keV and 1683-keV transitions both populating 11^- states. The depopulation of each one of the 11^- states contains transitions of very similar energies 1197-keV (from the state at $E_x = 9718$ keV) and 1239-keV (from the state at $E_x = 9760$ keV) both decaying to the 10^- state at $E_x = 8521$ keV of structure M-1. The two 11^- states respectively decay by a 2906-keV transition (from the $E_x = 9718$ keV state) and a 2949-keV transition (from the $E_x = 9760$ keV state), both decaying to the 6811 keV 9^- state and both with $R_{\text{DCO}} - E2 \approx 1.0$, which fixes the spin and parity of the 11^- states. Additional decay-out transitions connect this band from the state at $E_x = 13615$ keV 15^- with the M-4 structure (the transition with energy 2061 keV), and from the state at $E_x = 9718$ keV 11^- with the single-particle region (the 2906, 1447, and 454-keV transitions). Because of the described forking decay of the 13^- state at $E_x = 11443$ keV, it is not possible to state whether either of the mentioned 11^- states is the band head of the observed rotational structure built upon the latter state and stretching up to the state (19^-) at $E_x = 19238$ keV. Figure 7(a) shows a coincidence spectrum that suggests, by the balance of the intensities, the placement of the transitions in the odd-spin band. The spin assignment for the states 15^- at $E_x = 13615$ keV and 17^- at $E_x = 16194$ keV in WD-1 are justified by the $R_{\text{DCO}} - E2 \approx 1.0$ values of the 2173-keV $15^- \rightarrow 13^-$ and 2579-keV $17^- \rightarrow 15^-$ transitions. The spin and parity (19^-) of the state at $E_x = 19238$ keV is derived from the regularity of the band. The even-spin band stretches from its band head, the 10^- state at $E_x = 9622$ keV up to the (18^-) state at $E_x = 18131$ keV. The spin and parity 10^- of the state at $E_x = 9622$ keV level is based on the $E2$ character of its only decay-out transition 2785-keV $10^- \rightarrow 8^-$ connecting with the 8^- state at $E_x = 6837$ keV. The $R_{\text{DCO}} - E2 \approx 1.0$ values for the 1917-keV $14^- \rightarrow 12^-$ and 1498-keV $12^- \rightarrow 10^-$ transitions justify the values of 14^- and 16^- of the states at $E_x = 13037$ keV and 11120 keV. The spin and parity of the next two upper states are suggested by the regularity of the band.

2. Structure WD-2

The WD-2 structure is built up by seemingly collective states from 13^+ at $E_x = 13246$ keV up to 23^+ at $E_x = 22996$ keV, which corresponds to the highest reported excitation energy in this work. Figures 7(b) and 7(c) focus on this structure. The dipole character of the 2456-keV $13^+ \rightarrow$

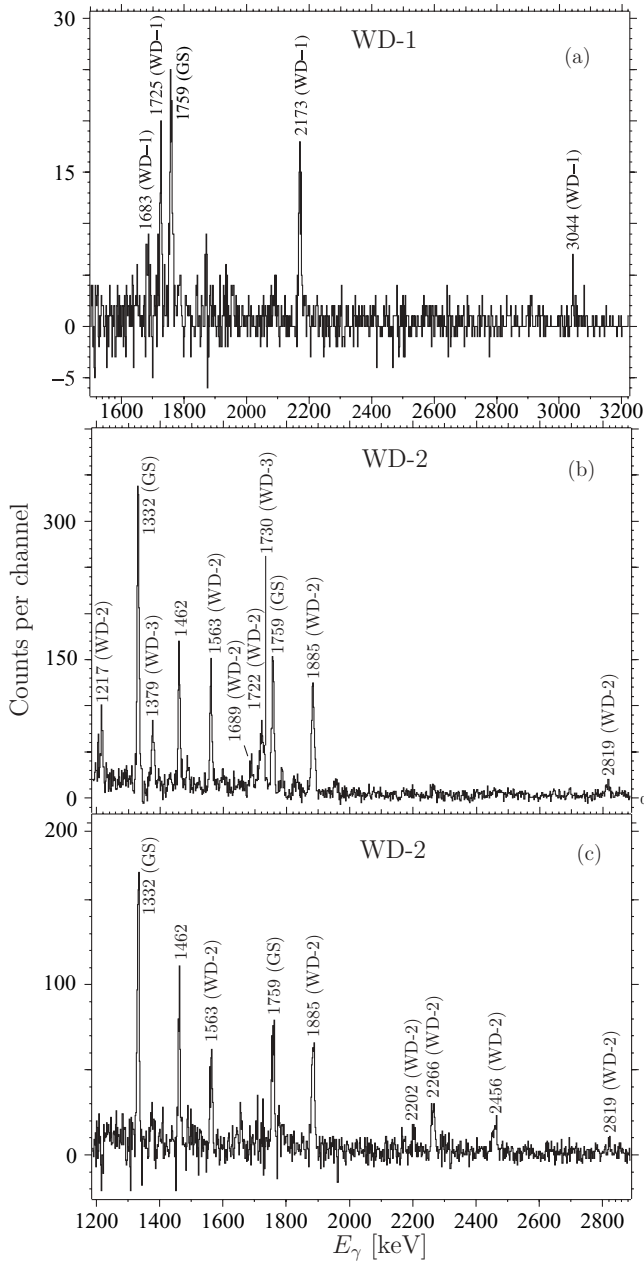


FIG. 7. (a) Spectrum in double coincidence with the 2579-keV $17^- \rightarrow 15^-$ transition and one of the 1725-keV or 2173-keV transitions in WD-1. (b) Spectrum in double coincidence with the 2266-keV $21^+ \rightarrow 19^+$ transition and one of the 1885-keV or 1563-keV transitions in WD-2. The 2819-keV $23^+ \rightarrow 21^+$ γ -ray is seen clearly. (c) Spectrum in double coincidence with the 1217-keV $15^+ \rightarrow 13^+$ transition and one of the 2266-keV, 1885-keV, or 1563-keV transitions in WD-2. See caption to Fig. 3 for additional explanations.

12^- transition fixes $I = 13\hbar$ for the WD-2 band head at $E_x = 13246$ keV. The assignment of 15^+ for the state at $E_x = 14463$ keV is based on the mixed $E2/M1$ character of the 1689-keV transition that depopulates that state and populates the 14^+ state at $E_x = 12775$ keV in the WD-3 structure, and by the $E2$ 1217-keV transition that populates the 13^+ state at $E_x = 13246$ keV.

3. Structure WD-3

Structure WD-3 corresponds to two apparent quadrupole collective bands. The first one has the states from 10^+ , at $E_x = 9665$ keV to (22^+) at $E_x = 22863$ keV, and the second one from (14^+) state at $E_x = 13282$ keV to (20^+) state at $E_x = 20018$ keV. Figure 8 illustrates this structure. The 10^+ state at $E_x = 9665$ keV is connected to the 6^+ state at $E_x = 4265$ -keV by five γ -ray sequences of two $E2$ transitions each. They populate several 8^+ states and subsequently decay to the $E_x = 4265$ keV, 6^+ state. As an example, the 2416-keV transition connects the states at $E_x = 9665$ keV, 10^+ and at $E_x = 7250$ keV, 8^+ , followed by the a 2986-keV, $8^+ \rightarrow 6^+$ transition. The 14^+ state at $E_x = 12775$ keV state is important because it justifies the 15^+ assignment for the state at $E_x = 14463$ keV in the WD-2 structure using the linking transition at 1689-keV, which has a mixed $E2/M1$ character. The spin

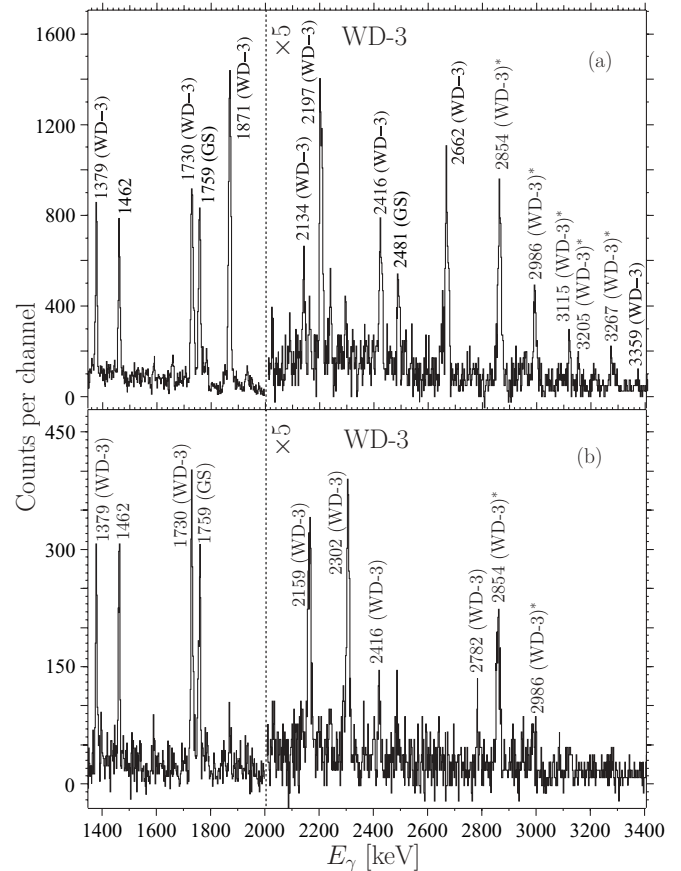


FIG. 8. (a) Spectrum in double coincidence constructed with the addition of the 2662-keV $20^+ \rightarrow 18^+$ and the 2197-keV $18^+ \rightarrow 16^+$ transitions and one of the 1730-keV or 1379-keV transitions in WD-3. (b) Spectrum in double coincidence constructed with the addition of the 2302-keV $18^+ \rightarrow 16^+$ and the 2159-keV $16^+ \rightarrow 14^+$ transitions and one of the 1730-keV or 1379-keV transitions in WD-3. For $E_\gamma \geq 2$ MeV the spectra have been multiplied by a factor to be compared with the low-energy region. See caption to Fig. 3 for additional explanations.

assignments (22^+) and (20^+) for the states on top of the WD-3 bands are given by the rotational regularities of the bands.

IV. THEORETICAL INTERPRETATIONS

A. Shell model interpretation

Since ^{60}Ni is magic in its proton number and has only four neutrons outside the $N = 28$ shell, it clearly calls for the spherical-shell model in order to interpret its low energy structures (GS, S-1, and S-2). The analysis using the spherical shell-model involves the $2p_{3/2}$, $1f_{5/2}$, and $2p_{1/2}$ shells above the $N, Z = 28$ gap (the so-called upper fp -shell) and the $1f_{7/2}$ shell below the gap. Though important as well, at present it is not possible to also include the positive parity $1g_{9/2}$ shell [39]. Large-scale shell-model calculations have been performed using the shell-model code ANTOINE [40] to interpret the low-energy positive-parity states in ^{60}Ni . The calculations were performed using the GXPF1A [41,42] and the KB3G [43] interactions. The configuration space was truncated to allow up to five-particle excitations, $t = 5$, from the $1f_{7/2}$ shell to the upper fp -shell. Bare g -factors and effective charges of $1.15e$ for protons and $0.8e$ for neutrons were used [44]. Experimental γ -ray energies were used to calculate branching ratios and state lifetimes. The results are summarized in Figs. 9, 10, 11, and Table III.

Figure 9 displays the neutron and proton occupation numbers as a function of angular momentum for the single-particle structures in ^{60}Ni . The results shown justify the neutron configuration of zero neutron-holes in the $1f_{7/2}$ shell. The plot for the proton occupation number shows that the difference

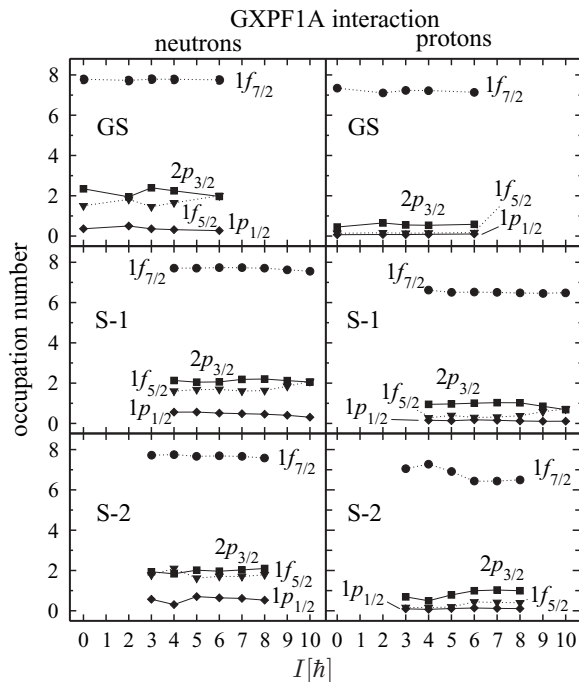


FIG. 9. Neutron and proton occupation numbers as a function of angular momentum for the single-particle structures in ^{60}Ni using the GXPF1A interaction.

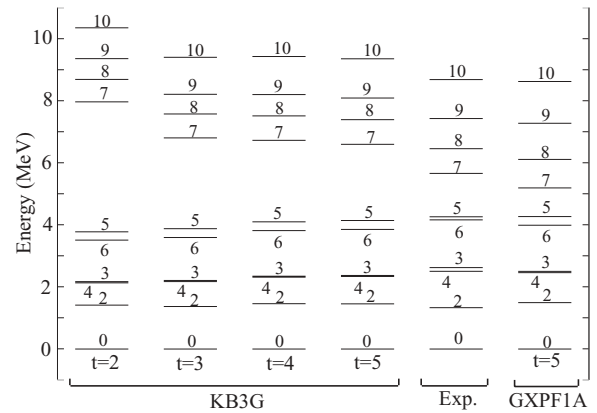


FIG. 10. Comparison between calculations using the KB3G interaction (first four columns to the left), the GXPF1A interaction (last column to the right), and the positive-parity experimental yrast states in ^{60}Ni . See text for details.

between the GS and the S-1, and S-2 structures is that one particle is promoted from the $1f_{7/2}$ shell to the $2p_{3/2}$ shell.

Theoretical and experimental energies for the yrast states are shown in Fig. 10. The labels on the lower part (KB3G, GXPF1A, and Exp.) give the name of the interactions used to perform the large-scale shell-model calculations and the corresponding experimental result for this work. The theoretical calculations use different numbers of particles excited from the lower $1f_{7/2}$ shell to the upper fp -shell. The KB3G results indicate convergence of the calculation at five active particles, since there is no significant difference between the calculations with $t = 4$ and $t = 5$. The results with the GXPF1A interaction fit well the state with $I = 10\hbar$ and reduce the gap between the $I = 5\hbar$ and $I = 7\hbar$ states, (this gap is predicted higher according to the KB3G interaction) although the GXPF1A interaction overestimates the reduction in comparison with the experiment.

For the following discussion the GXPF1A interaction is used. In order to compare experimental and theoretical level schemes, the theoretical states are shifted against the experimental ones by an amount called Binding Energy Shift (BES) such that the square of the mean quadratic deviation, the

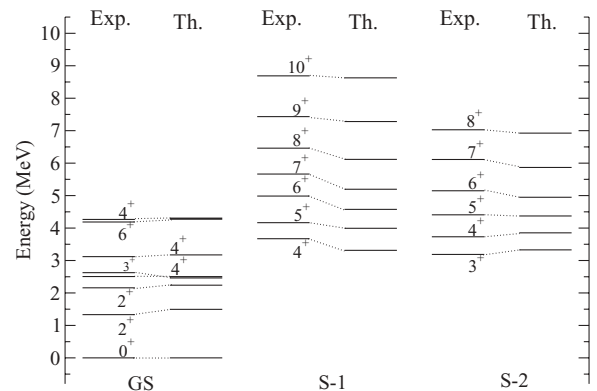


FIG. 11. Comparison between the calculations using the GXPF1A interaction and experimental data for the structures GS, S-1, and S-2 in ^{60}Ni . See text for details.

TABLE III. Comparison of the available experimental data for ^{60}Ni with shell-model (GXPF1A) calculations for the GS, S-1, and S-2 structures. The table shows γ -ray branching ratios (b) and mixing ratios (δ) as well as lifetimes of the states (τ). The experimental lifetimes are taken from the compilation of Ref. [38]. The experimental values for the mixing ratio, δ_{exp} , are shown for some transitions with $\Delta I=1$ and $\Delta I=0$.

E_x [keV]	E_γ [keV]	I_i^π [\hbar]	I_f^π [\hbar]	b_{exp}	b_{theo}	δ_{exp}	δ_{theo}	τ_{exp} [ps]	τ_{theo} [ps]
Structure GS									
1332.6(2)	1332.5(2)	2 ⁺	0 ⁺	1.00(0)	1.00		0.0	1.11(6)	0.97
2158.9(2)	826.1(2)	2 ⁺	2 ⁺	0.87(2)	0.35	0.2(2)	-0.58	0.85(25)	0.68
	2159.0(3)	2 ⁺	0 ⁺	0.13(2)	0.65		0.0		
2505.8(2)	346.8(4)	4 ⁺	2 ⁺	0.00(1)	0.0		0.0	4.8(14)	2.62
	1173.2(2)	4 ⁺	2 ⁺	1.00(1)	1.0		0.0		
2626.1(2)	119.6(1)	3 ⁺	4 ⁺	0.19(4)	0.01		0.09	0.6($\frac{5}{3}$)	8.08
	467.1(1)	3 ⁺	2 ⁺	0.56(5)	0.05	-0.38(18)	1.0		
	1293.7(2)	3 ⁺	2 ⁺	0.25(4)	0.94	-0.11(15)	1.2		
3119.5(2)	493.4(1)	4 ⁺	3 ⁺	0.11(2)	0.07	-0.65 < δ < 0.14	-0.02	0.35(14)	0.30
	613.7(3)	4 ⁺	4 ⁺	0.04(1)	0.00		-5.2		
	1787.3(3)	4 ⁺	2 ⁺	0.85(3)	0.93		0.0		
4265.0(2)	1145.2(2)	6 ⁺	4 ⁺	0.07(1)	0.08		0.0	0.7($\frac{2}{3}$)	0.33
	1759.2(3)	6 ⁺	4 ⁺	0.93(1)	0.92		0.0		
Structure S-1									
3671.2(2)	1165.2(2)	4 ⁺	4 ⁺	0.98(2)	0.87	+0.10(8), -1.4(5)	-0.09	0.09(6)	0.08
	1512.1(6)	4 ⁺	2 ⁺	0.02(2)	0.0		0.0		
4165.6(2)	494.4(2)	5 ⁺	4 ⁺	0.06(2)	0.15		-0.19	1.2(6)	0.54
	1044.4(2)	5 ⁺	4 ⁺	0.10(3)	0.30		-0.43		
	1539.0(3)	5 ⁺	3 ⁺	0.10(3)	0.0		0.0		
	1659.6(3)	5 ⁺	4 ⁺	0.73(6)	0.55	0.3 < δ < 2.0	0.99		
5662.7(3)	514.4(2)	7 ⁺	6 ⁺	0.05(1)	0.02		0.11	1.0($\frac{30}{4}$)	0.30
	677.7(2)	7 ⁺	6 ⁺	0.49(4)	0.32	-0.35 < δ < -0.02	-0.23		
	1255.1(3)	7 ⁺	5 ⁺	0.11(2)	0.02		0.0		
	1397.7(2)	7 ⁺	6 ⁺	0.33(4)	0.51	0.12(13)	-0.22		
	1498.0(4)	7 ⁺	5 ⁺	0.02(1)	0.14		0.0		
6461.0(3)	348.7(2)	8 ⁺	7 ⁺	0.06(2)	0.02		0.03	1.7($\frac{23}{7}$)	0.35
	798.1(2)	8 ⁺	7 ⁺	0.63(4)	0.63	-0.45(5)	-0.29		
	1312.4(4)	8 ⁺	6 ⁺	0.17(2)	0.13		0.0		
	1475.0(4)	8 ⁺	6 ⁺	0.10(1)	0.07		0.0		
	2195.9(5)	8 ⁺	6 ⁺	0.04(1)	0.16		0.0		
7433.2(3)	972.3(2)	9 ⁺	8 ⁺	0.68(8)	0.78	-0.4(2)	-0.29		0.17
8688.8(4)	1255.4(4)	10 ⁺	9 ⁺	0.55(10)	0.80	-0.5(3)	-0.29		0.06
Structure S-2									
3186.8(2)	680.0(1)	3 ⁺	4 ⁺	0.27(11)	0.38		-0.11	0.20(6)	0.77
	1028.2(2)	3 ⁺	2 ⁺	0.45(12)	0.23		-0.82		
	1854.0(2)	3 ⁺	2 ⁺	0.27(11)	0.39		-0.58		
3730.7(2)	545.0(1)	4 ⁺	3 ⁺	0.10(4)	0.03		-0.33	0.3($\frac{4}{1}$)	0.82
	610.9(3)	4 ⁺	4 ⁺	0.10(4)	0.11		-0.05		
	1105.0(4)	4 ⁺	3 ⁺	0.17(5)	0.12		0.38		
	1224.9(2)	4 ⁺	4 ⁺	0.24(9)	0.38		0.19		
	2398.0(3)	4 ⁺	2 ⁺	0.38(10)	0.33	-0.05 < δ < 0.4	0.0		
4407.5(2)	241.8(1)	5 ⁺	5 ⁺	0.15(3)	0.03		-0.01		0.33
	676.6(2)	5 ⁺	4 ⁺	0.34(5)	0.12		0.08		
	736.4(2)	5 ⁺	4 ⁺	0.21(4)	0.03		-0.77		
	1288.3(4)	5 ⁺	4 ⁺	0.04(1)	0.12		-1.57		
	1781.3(3)	5 ⁺	3 ⁺	0.10(2)	0.02		0.0		
	1901.7(3)	5 ⁺	4 ⁺	0.16(3)	0.61		5.55		
5148.4(3)	740.9(2)	6 ⁺	5 ⁺	0.47(6)	0.04	-0.4(1)	-0.22		0.11
	883.5(1)	6 ⁺	6 ⁺	0.13(3)	0.22		-0.03		
	982.9(3)	6 ⁺	5 ⁺	0.06(2)	0.61		-0.27		
	1477.3(4)	6 ⁺	4 ⁺	0.02(1)	0.04		0.0		

TABLE III. (*Continued.*)

E_x [keV]	E_γ [keV]	I_i^π [\hbar]	I_f^π [\hbar]	b_{exp}	b_{theo}	δ_{exp}	δ_{theo}	τ_{exp} [ps]	τ_{theo} [ps]
6112.2(4)	2029.0(5)	6 ⁺	4 ⁺	0.03(1)	0.05		0.0		
	2643.0(4)	6 ⁺	4 ⁺	0.28(5)	0.04		0.0		
	963.7(3)	7 ⁺	6 ⁺	0.53(5)	0.57	-0.3(2)	-0.20		0.07
	1847.2(5)	7 ⁺	6 ⁺	0.32(4)	0.14		0.14		
7027.5(3)	1946.6(5)	7 ⁺	5 ⁺	0.15(3)	0.28		0.0		
	914.8(3)	8 ⁺	7 ⁺	0.19(5)	0.65		-0.19		0.14
	1365.0(2)	8 ⁺	7 ⁺	0.27(6)	0.06		-0.05		
	1578.6(4)	8 ⁺	6 ⁺	0.16(4)	0.0		0.0		
	1880.9(5)	8 ⁺	6 ⁺	0.27(7)	0.25		0.0		
	2041.9(5)	8 ⁺	6 ⁺	0.11(6)	0.03		0.0		

so called Mean Level Deviation (MLD), is minimized. A total of 30 states were calculated and only six calculated states have been excluded from the comparison, namely those for which we could not identify the experimental counterparts. Note that the assignment of calculated levels to experimentally observed ones is not solely based on matching excitation energies or sequences of states with the same spin and parity, but also on observed decay branches—in particular, if calculated levels of the same spin and parity lie close in energy. The present study includes the positive-parity states up to the 10^+ state at $E_x = 8689$ keV where the spherical shell model is expected to do well. In this work a MLD of 179 keV and a BES of -98 keV were obtained. In Fig. 11 the theoretical levels are compared with the experimental ones of the GS, S-1, and S-2 structures. The evaluation of the agreement on electromagnetic decay properties between theory and experiment is achieved by calculating the Mean Branching Deviation (MBD) [45]. Perfect agreement gives $\text{MBD} = 0.0$ whereas a fully reversed decay pattern gives $\text{MBD} = 1.0$. Intermediate values as $\text{MBD}_i(4_2^+) = 0.036(1)$, and $\text{MBD}_i(2_2^+) = 0.5(1)$ are considered good and bad agreements respectively. These values show that the average value obtained for the known yrast sequence, $\text{MBD} = 0.13(1)$ represent a very good agreement. Besides a good agreement between branching ratios and mixing ratios, lifetimes are in general well reproduced although with some notable exceptions as observed in Table III. Some examples for this good agreement can be observed in the calculated and experimental lifetimes for the 4^+ state at $E_x = 3120$ keV, which are 0.30 ps and 0.35(14) ps respectively; the mixing ratio values $\delta(E2/M1)$ for the 678-keV $7^+ \rightarrow 6^+$ transition which depopulates the state at $E_x = 5663$ keV, agree within error bars. Some of the exceptions for this good agreement are the states 3^+ at $E_x = 2626$ keV and 3^+ at $E_x = 3186$ keV in the structure S-2, for example. Regarding the former state, for its 467-keV $3^+ \rightarrow 2^+$ depopulating transition $B(M1; 3^+ \rightarrow 2^+)_{\text{theo.}} = 0.0$ Weisskopf units (W.u.), whereas the experimental value is $0.29^{(1.18)}_{(0.24)}$ W.u. Regarding the same state, for its 120-keV transition, $B(M1; 3^+ \rightarrow 4^+)_{\text{theo.}} = 0.016$ W.u. whereas the experiment gives $5.8^{(26.5)}_{(5.3)}$ W.u. These differences produce an enormous discrepancy: $\tau_{\text{theo}} = 8.08$ ps, whereas $\tau_{\text{exp}} = 0.6^{(5)}_3$ ps [21] that can be produced by any or a mixing of different reasons. From the theoretical point of view small $M1$ or $E2$ matrix elements can be affecting

the result for these particular states, which may be related with a probable vibrational character of the states, which the shell model is not able to describe. On the other hand, modern RDDS lifetime measurements have changed drastically old values in different mass regions [46,47]. Our present results are a clear motivation to review experimentally the lifetimes of excited states in ^{60}Ni with modern techniques.

B. Cranked Nilsson-Strutinsky interpretation

The rotational states are interpreted in the framework of the configuration-dependent cranked Nilsson-Strutinsky (CNS) approach [48–50] using the standard Nilsson parameters [49]. Pairing will only have a small effect on the results due to the general high spins and high excitation energies of the structures studied.

The most important orbitals for a theoretical description of ^{60}Ni include the $\mathcal{N} = 3$ high- j $1f_{7/2}$ and the upper fp -shell orbits $1f_{5/2}$, $2p_{3/2}$, and $2p_{1/2}$, and finally the $\mathcal{N} = 4$ orbit $1g_{9/2}$. In the deformed rotating potential considered here, these j -shells will mix, i.e., the wave functions of the single-particle orbitals will have amplitudes in several j -shells. However, it turns out that if the deformation is not too large, these orbitals can be classified as having their main amplitudes in either the high- j intruder shell or in the other shells with lower j -values, see Refs. [48,51]. For example, in the $\mathcal{N} = 3$ shell, the orbitals will either be dominated by the high- j $1f_{7/2}$ shell or by the other j -shells which means that they can be characterized as being of $1f_{7/2}$ character or of $1f_{5/2}$, $2p_{3/2}$ (in short fp) character (for ^{60}Ni , the Fermi surface will fall far below the $2p_{1/2}$ shell so this shell will not contribute significantly to the wave functions of the occupied orbitals). The classification into high- j and low- j orbitals is only possible if so-called virtual crossings between weakly interacting orbitals are first removed. The classification is made easier by the use of the eigenstates of the rotating oscillator potential as basis states where the weak coupling between the different shells in this potential is neglected, see Ref. [49] for details.

As an example, Fig. 12 shows the calculated single-particle orbitals (Routhians), for neutrons as a function of the rotational frequency for typical deformation parameters $\epsilon_2 = 0.26$ and $\gamma \sim 20^\circ$. In this figure, the spherical origin of the different orbitals is indicated but, as explained above, it is not really

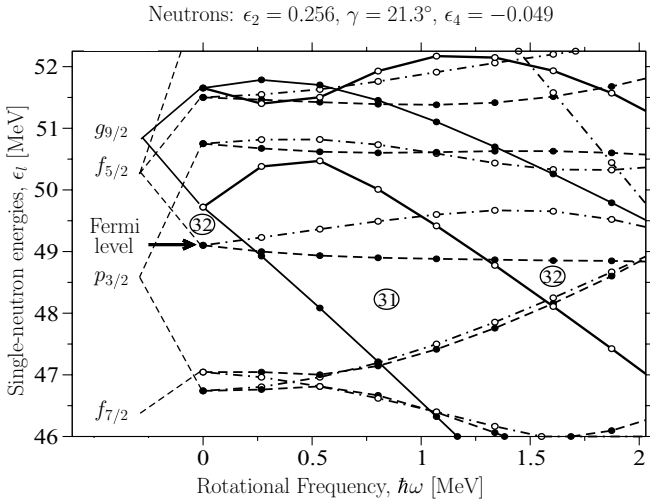


FIG. 12. Routhians calculated for neutrons at a typical mean deformation in ^{60}Ni . Solid (dashed) lines represent orbits with parity $\pi = +$ ($\pi = -$), filled (open) dots represent orbits with signature $\alpha = 0$ ($\alpha = 1$). See text for details.

possible to make a distinction between $1f_{5/2}$ and $2p_{3/2}$ orbitals. Note also that two orbitals of $1f_{7/2}$ and fp character, respectively, come close in the lower part of the diagram which probably means that they will mix strongly. Our interest is however mainly the high-spin region, and it is then satisfactory to note that these orbitals split apart for frequencies larger than 0.5 MeV, where the up-sloping orbital has the expected properties of the highest $1f_{7/2}$ orbital while the lower orbital can be characterized as being of fp character. Due to the low Coulomb effects, the single-particle orbitals for protons and neutrons are almost identical. The main difference is the Fermi energy, which is higher for neutrons than for protons. Note the large signature splitting of the lowest high- j $1g_{9/2}$ intruder orbital which means that for configurations with one $1g_{9/2}$ neutron (or proton), one should expect only to observe the favoured signature. Furthermore, a large energy gap is formed at particle number 31 at $\hbar\omega \sim 1$ MeV in the Routhian diagram. Favoured configurations for $N = 32$ at this deformation will then be formed with all orbitals below the $N = 31$ gap filled and with the 32nd neutron in either signature of the (fp) orbital situated above the $N = 31$ gap. The ^{60}Ni configurations can then be written as

$$\begin{aligned} & \pi[(1f_{7/2})^{-p_1}(1g_{9/2})^{p_2}(fp)^{p_3}] \\ & \otimes \nu[(1f_{7/2})^{-n_1}(1g_{9/2})^{n_2}(fp)^{n_3}], \end{aligned} \quad (6)$$

with $p_1(n_1)$ being the number of proton (neutron) holes in orbitals of $1f_{7/2}$ character, $p_2(n_2)$ the number of protons (neutrons) in orbitals of $1g_{9/2}$ character, and $p_3(n_3)$ the number of particles in orbitals of ($f_{5/2}$, $p_{3/2}$) character (or “ fp -shell”). Since ^{60}Ni has four neutrons outside the doubly magic closed core ^{56}Ni ,

$$p_3 = p_1 - p_2; \quad n_3 = 4 + n_1 - n_2. \quad (7)$$

Because of these identities, it is sufficient to label the configurations of the deformed bands using the notation $[p_1 p_2, n_1 n_2]$. For example, the label $[31, 01]$ for the band

WD-2 implies that its assigned configuration corresponds to $p_1 = 3$ proton-holes in the $1f_{7/2}$ shell, $p_2 = 11g_{9/2}$ protons, $n_1 = 01f_{7/2}$ neutron-holes, and $n_2 = 11g_{9/2}$ neutrons.

The calculated energies are Strutinsky renormalized [52] to the rotating liquid-drop energy in the same way as introduced in Ref. [50]. This means that the resulting energies can be compared with the experimental ones on an absolute scale. A quantitative comparison is however only meaningful at high spins, i.e., $I \geq 10\hbar$ in the $A \approx 60$ region, because pairing is neglected in the calculations. The parameters of the static liquid drop are taken from the Lublin-Strasbourg drop (LSD) formula [53] while the rigid-body moment of inertia is calculated from a mass distribution with a diffuse surface [54], defined by the radius parameter $r_0 = 1.16$ fm and the diffuseness constant, $a = 0.6$ fm [50]. When comparing theoretical predictions with experimental data, the energies are shown relative to the rotating liquid-drop energy (minimized with respect to deformation) with the parameters specified above. This is exemplified in Fig. 13 where the energies for the magnetic structures of ^{60}Ni are displayed as a function of spin in the upper panels. The lower panel provides the energy difference between the associated theoretical and experimental bands. A perfect agreement corresponds to a vanishing energy difference but it is also of interest to note that a constant energy difference means that the relative energies (the transition energies) within a band are reproduced by the calculations.

1. Structure M-1

Experimentally, the M-1 structure is built on a 9^- band head, and has been observed up to spin 15^- with strong

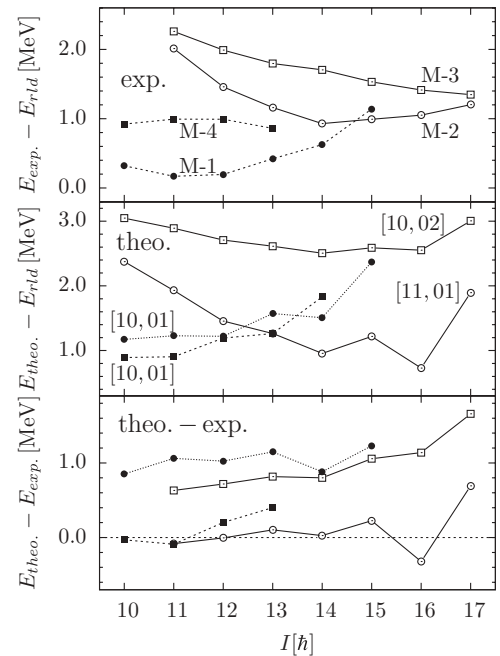


FIG. 13. Experimental (top panel) and CNS calculated (middle panel) energies and their differences (lower panel) for the magnetic structures in ^{60}Ni . The energies in the two upper panels are shown relative to the rotating liquid-drop energy [50]. Proposed structures share the same symbols.

dipole transitions. Because of the dipole character of the band, one may conclude that it has a hole in $1f_{7/2}$ orbitals while the negative parity is created with one $1g_{9/2}$ particle. Then, because of the neutron excess, the only reasonable interpretation is that the hole is created in a proton orbital while the $1g_{9/2}$ particle must be a neutron. This agrees with the $[10, 01]$ configuration calculated as yrast, specifically,

$$\pi[(1f_{7/2})^{-1}(fp)^1] \otimes \nu[(1g_{9/2})^1(fp)^3], \quad (8)$$

where the coupling of the fp neutrons to a maximum spin of $9/2\hbar$ (corresponding to $\alpha = +1/2$) is favored (according to the single-particle diagram). This means that the fp proton contributes to a maximum spin of $5/2\hbar$ ($\alpha = +1/2$), and in this way, a maximum spin of $3.5 + 2.5 + 4.5 + 4.5 = 15\hbar$ is obtained, i.e. the band is observed to termination. The band head is described as triaxial with deformation parameters $\epsilon_2 = 0.21$ and $\gamma = 22^\circ$. Figure 13 shows that the binding energy is underestimated by approximately 1 MeV while the trend of the energy levels with spin is well reproduced.

The states in this band are obtained from collective rotation and by the alignment of the angular momentum component produced by the $1f_{7/2}$ proton-hole with the main spin axis. This kind of coupling creates a large magnetic-moment component perpendicular to the direction of the total nuclear spin which gives rise to strong magnetic-dipole transitions. As the band approach termination, the individual spin vectors align, which leads to a decrease in strength of the magnetic-dipole transitions (see Sec. IV B4). The electric quadrupole transitions are sensitive to the deformation and are expected to decrease as the collective contribution to the $B(E2)$ values eventually disappears at the terminating state. Both these effects are present in the experimental $B(M1)/B(E2)$ ratios and the observed decrease seen for the highest values suggests that the $B(M1)$ values are decreasing more rapidly than the $B(E2)$ values. This mechanism of angular momentum generation is similar to the shears mechanism [18], in which the high-spin states are produced by the simultaneous alignment between proton and neutron spin vectors around a non-principal axis. This is slightly different from our case with a relatively large collective component and a smaller perpendicular component built mainly by the $1f_{7/2}$ proton-hole.

2. Structures M-2 and M-3

Structures M-2 and M-3 are both built on 11^+ band heads, have positive parity, have been observed up to $I^\pi = 17^+$, and similar to the M-1 band, have dipole character. The positive parity of the bands is given by the even number of particles in the $\mathcal{N} = 3$ major shell. Their magnetic character (i.e., strong magnetic-dipole transitions) can be built with one $1f_{7/2}$ proton hole, i.e., $(f_{7/2})^{-1}(g_{9/2})^2$. There are two possibilities, the configuration $[10, 02]$,

$$\pi[(1f_{7/2})^{-1}(fp)^1] \otimes \nu[(1g_{9/2})^2(fp)^2], \quad (9)$$

or the configuration $[11, 01]$,

$$\pi[(1f_{7/2})^{-1}(1g_{9/2})^1] \otimes \nu[(1g_{9/2})^1(fp)^3]. \quad (10)$$

In both cases, two magnetic bands can be formed considering the two signatures of the (fp) proton and the three (fp) neutrons, respectively. There are, however, some difficulties in the assignment of the configurations for the M-2 and M-3 bands. We assign tentatively the lowest band, M-2, to the lowest calculated $[11, 01]$ configuration. In the two upper panels of Fig. 13 the problem that this interpretation offers can be seen: the calculated band exhibits a sizeable signature splitting at high spin that does not appear in the experimental data. Regarding the M-3 band there are then two possibilities, first, to assign it to the next higher $[11, 01]$ configuration, which is still lower than the lowest $[10, 02]$ configuration. However, this does not seem to be the case because of two problems: first, the calculated energies for the 16^+ and 17^+ states are too high, and second, the large calculated signature splitting is not observed in the experimental band. We assign therefore band M-3 to the lowest $[10, 02]$ band, as it is reported in Fig. 13. It is apparent immediately that the two calculated bands $[11, 01]$ and $[10, 02]$, are rather different whereas the experimental M-2 and M-3 bands look much more similar. One way out of these problems is to assign both, M-2 and M-3, as $[10, 02]$, because the two $[10, 02]$ bands are calculated close in energy (~ 200 keV apart) and they both show small signature splitting. The main problem then is the high calculated excitation energy, which could be lowered by lowering the $1g_{9/2}$ neutron shell relative to the $1g_{9/2}$ proton shell. Such a lowering has already been discussed in connection with the superdeformed band in ^{62}Zn [55].

In this context, one should note that the $I_{\max} - 1$ state will include some spurious components due to the cranking approximation as discussed in Ref. [56]. The restoration of the broken rotational symmetry will lead to an increase of the energy of the $I_{\max} - 1$ state. Consequently, the energy staggering close to termination will decrease and come closer to experiment for all the calculated configurations shown in Fig. 13. However, the wave-functions are distributed over more shells and the deformations are larger for the present ^{56}Ni configurations than for the configurations considered in Ref. [56]. Therefore, the spurious components and the associated energy corrections are probably rather small for the magnetic structures in ^{60}Ni .

3. Structure M-4

Structure M-4 is built on a 9^- band head and has been observed up to $I^+ = 13^-$. It has similar characteristics as the M-1 band, indicating that it is built from the same type of configurations, i.e. with one $1f_{7/2}$ proton hole and one $1g_{9/2}$ neutron particle. As can be seen in Fig. 13, the energy values for the states in the M-4 band are predicted higher than for the states in the M-1 structure. The negative parity of the structure is given by the odd number of neutrons in the fp shell. The band head has a deformation of $\epsilon_2 \approx 0.21$ and $\gamma \approx 30^\circ$. The magnetic character can be constructed with the same $[10, 01]$ configuration indicated in Eq. (8) for band M-1, i.e., one $1f_{7/2}$ proton hole and one $1g_{9/2}$ neutron particle. With the present interpretation, the two $[10, 01]$ bands where the fp neutrons couple to a maximum spin of $11/2\hbar$ ($\alpha = -1/2$) are

not observed. This is as would be expected because they are calculated approximately 1 MeV higher in energy than the two bands shown in Fig. 13.

4. Many-particle-plus rotor calculations for the [10,02] configuration.

As in the M-1 structure the strong $M1$ transitions in bands M-2 and M-3 are produced by the alignment of angular momentum of the $1f_{7/2}$ proton hole with the total angular momentum vector. In order to investigate the magnetic features of these bands many-particle-plus rotor calculations were performed for the configuration [10,02]. The particle-space was selected to consist of single-particle states obtained from the deformed modified oscillator potential. These orbitals can be divided into three parts, orbits of $1f_{7/2}$ character, the remaining $\mathcal{N} = 3$ orbitals and orbits of $1g_{9/2}$ character. In the calculations the $\pi[(1f_{7/2})^7(fp)^1]\nu[(1g_{9/2})^2]$ part of the configuration was treated microscopically. No additional excitations between the $1f_{7/2}$ and the fp shells were allowed which means that the mixing between these deformed shells induced by the rotation was neglected. Effective parameters for the remaining core part were obtained in a similar way as in Ref. [57]. Moments of inertia of the core were estimated using cranking calculations along each principal axis and effective g_R -factors and quadrupole moments (Q_0 and Q_2) for the core were estimated using cranking around the main rotational axis. Three different values of γ (0° , 15° , 30°) for a constant value of $\epsilon_2 = 0.25$ were used in the calculations. The values of the parameters used in the calculations are shown in Table IV. The results for $B(M1)$, $B(E2)$ and the $B(M1)/B(E2)$ ratios are shown in Fig. 14. The $B(M1)$ values are rather similar for the three deformations and decrease with increasing angular momentum as discussed in Sec. IV B 1. The $B(E2)$ values on the other hand are rather constant with spin (except for the signature staggering seen in the $\gamma = 0^\circ$ curve) but decrease with increasing γ values. The resulting $B(M1)/B(E2)$ ratios are in the same order as the experimental values obtained for the M-1 and M-2 bands displayed in Fig. 6. Another interesting feature of the calculations is that we can expect such values as $B(E2) = 0.01(eb)^2$ and $B(M1) = 1.0\mu_N^2$ for the magnetic structures. Experimental values of the $B(M1)/B(E2)$ ratios for the M-3 band were not possible to obtain because cross-

TABLE IV. Parameters used for the calculations of the [10,02] configuration. The indices 1,2,3 refer to the body-fixed frame. In the case of axial symmetry ($\gamma = 0^\circ$), the three axis is the symmetry axis. In addition to these parameters $g_s = 0.7g_s^{\text{free}}$ was used.

γ	g_R	Q_0^a		Q_2		
		[fm ⁻²]		[MeV/ \hbar]		
0°	-0.146	36.804	0.0	0.14061	0.14061	
15°	-0.126	35.304	-5.443	0.13407	0.14420	3.04676
30°	-0.099	30.977	-10.681	0.13256	0.14993	0.77033

^a Q_0 and Q_2 follow the convention described in Ref. [58].

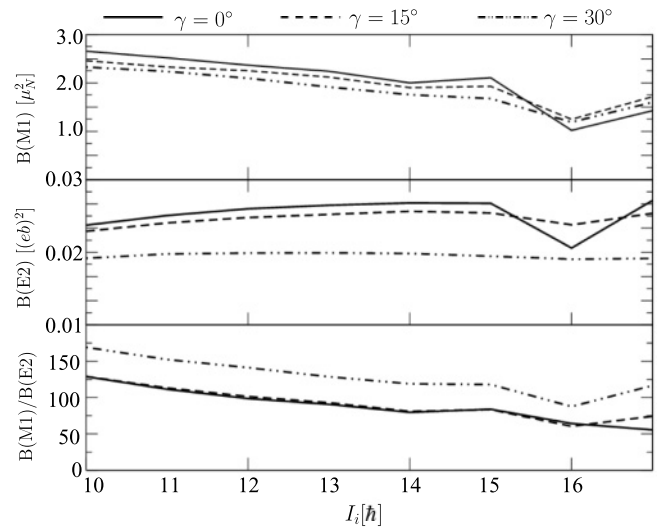


FIG. 14. Theoretical values for $B(M1)$ (upper panel), $B(E2)$ (central panel) and $B(M1)/B(E2)$ (lower panel), calculated for a constant deformation parameter of $\epsilon_2 = 0.25$ and three values for γ (0° , 15° , 30°) for the configuration [10,02] using many-particle-plus rotor calculations. As a reference, two deformation parameters (ϵ_2, γ) calculated for the [10,02] configuration using the CNS formalism at $I = 10$ and $16\hbar$ are $(0.220, 9.1^\circ)$ and $(0.20, 58.5^\circ)$, respectively. See text for details.

over quadrupole transitions between pairs of states were not observed.

5. Structure WD-1

The fact that the WD-1 structures are “nonmagnetic” suggests that they have an even number of proton and neutron $1f_{7/2}$ holes. Furthermore, the negative parity shows that they have an odd number of $1g_{9/2}$ particles. Then, because they have been observed up to spin $I = 19\hbar$, we may conclude that they should be assigned to the [20,01] configuration,

$$\pi[(1f_{7/2})^{-2}(fp)^2] \otimes \nu[(1g_{9/2})^1(fp)^3]. \quad (11)$$

In agreement with experiment, two bands at similar energies are formed, where the two bands are distinguished by the signatures of the 3 fp particles.

Figure 15 shows a good agreement between prediction and experiment for the evolution of the bands with spin. One could note that the maximum spin which can be reached in this configuration is $I_{\text{max}} = 20\hbar$ but the highest spin observed is $I = 19\hbar$. Figure 16 displays the shape trajectories of the four well-deformed structures. Regarding the WD-1 bands it is rather surprising that they follow fairly parallel in the energy-spin plot (Fig. 15) but their deformation trajectories are different (Fig. 16). Thus, the favored band (odd spins) rotates collectively at $I = 11\hbar$ but evolves to single-particle rotation, being (essentially) fully aligned at $I = 19\hbar$. The unfavored band (even spin) on the other hand stays more collective and starts to interact with a [20,11] band before reaching the I_{max} state $I = 20\hbar$. There is thus a smooth transition to the [20,11] configuration and the band can be followed continuously to the termination of this configuration at $I = 24\hbar$.

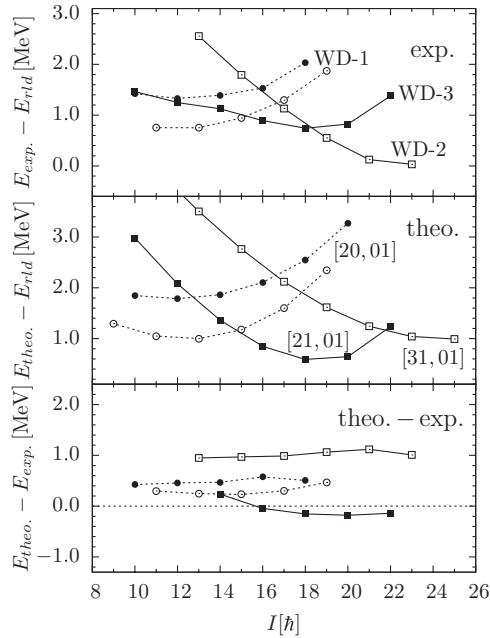


FIG. 15. Experimental (top panel) and CNS calculated (middle panel) energies and their differences (lower panel) for the well deformed structures in ^{60}Ni . The energies in the two upper panels are shown relative to the rotating liquid-drop energy [50].

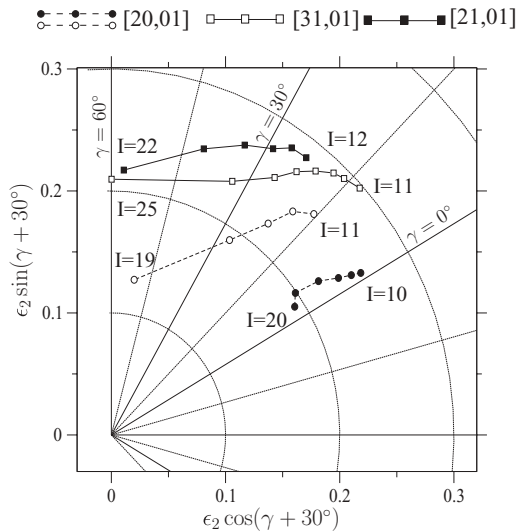


FIG. 16. Shape trajectory for the structures with the configurations [20,01]—WD-1, [31,01]—WD-2, and [21,01]—WD-3. In this diagram, the $\gamma = 60^\circ$ axis represents single-particle rotation at oblate shape, where the single-particle angular momentum projection along the oblate symmetry axis (the rotation axis) is a preserved quantum number and the total angular momentum is obtained as the sum of all these components. Going away from the $\gamma = 60^\circ$ axis, the nucleus becomes more and more asymmetric relative to the rotation axis and the rotation becomes increasingly collective. Especially, the $\gamma = 0^\circ$ axis corresponds to prolate shape with rotation around the perpendicular axis. The different trajectories show typical features of fixed unpaired configurations at small or intermediate deformation, being more or less collective at low spin but slowly approaching the non-collective limit and terminating at their I_{max} values if they do not mix with other configurations.

6. Structure WD-2

The WD-2 positive-parity band has the largest spin value observed in this work, $I = 23\hbar$. In order to get positive parity and high enough spin values, two particles have to be promoted to the $1g_{9/2}$ shell. The most likely configuration is [31,01],

$$\pi[(1f_{7/2})^{-3}(1g_{9/2})^1(fp)^2] \otimes \nu[(1g_{9/2})^1(fp)^3]. \quad (12)$$

This interpretation is also strengthened by the fact that all other configurations which extend to $I = 23^+$ are calculated at least 1 MeV higher in energy. The signature partner obtained from changing the signature of the odd $1f_{7/2}$ proton is calculated close in energy for spin values up to $I = 20\hbar$ but comes considerably higher in energy before it terminates at $I = 24\hbar$. Therefore, it is not strange that only the odd spin partner is observed in the present experiment.

The odd spins of the band implies that both the $\alpha = +1/2$ signature of the fp neutrons, and the $\alpha = -1/2$ signature of the $1f_{7/2}$ proton holes are favored. In this scheme $I_{\text{max}} = 25\hbar$. The band has been observed up to $I = 23\hbar$, i.e., according to the CNS calculations of Fig. 16, one transition short of termination. At its lowest spins the [31,01] structure is slightly triaxial ($\gamma \approx 15^\circ$) and well deformed ($\epsilon_2 \approx 0.3$) before it evolves toward smaller deformation and single-particle rotation at $\gamma \approx 60^\circ$.

7. Structure WD-3

Structure WD-3, similar to structure WD-2 has positive parity, is formed by a set of $E2\gamma$ -ray transitions, and has been seen up to similar excitation energy and spin, $I = 22\hbar$, a value that can be reached with only two $1f_{7/2}$ holes. The likely configuration is thus $(f_{7/2})^{-2}(g_{9/2})^2$, or [21,01],

$$\pi[(1f_{7/2})^{-2}(1g_{9/2})^1(fp)^1] \otimes \nu[(1g_{9/2})^1(fp)^3]. \quad (13)$$

Compared with the M-1 band, this configuration has one proton lifted from $1f_{7/2}$ to $1g_{9/2}$, where the coupling of the fp neutrons to a maximum of $9/2\hbar$ ($\alpha = 1/2$) is favored (according to the single-particle diagram, Fig. 12), while the odd fp proton has signature $\alpha = 1/2$. Except for the odd-spin signature partner ($\alpha = -1/2$ for the fp proton), all other positive-parity bands are calculated more than 1 MeV higher in energy for spin values $I \approx 20\hbar$. Figure 16 shows that configuration [21,01] has a similar deformation trajectory as [31,01] to oblate shape and single-particle rotation at its highest spin.

Experimentally band WD-3 forks at spins $I = 10, 12, 14\hbar$ to a parallel positive-parity structure that has been observed up to $I = (20)\hbar$. We have not been able to find any configuration which reproduces this structure.

V. CONCLUSIONS

A very extensive high-spin level scheme of ^{60}Ni has been presented. Normalized to mass, the ^{60}Ni level scheme of Fig. 1 is one of the most comprehensive high-spin level schemes ever deduced. Due to the combination of data from three experiments that used the very efficient γ -ray

spectrometer GAMMASPHERE and selective devices such as LUWUSIA and MICROBALL, a considerable amount of new experimental information has been extracted. Seven structures represented by more than 270 γ -ray transitions were placed in the ^{60}Ni level scheme. Each structure has been studied in detail both experimentally and theoretically. At low spin and low excitation energy relatively simple spherical shell-model calculations in the fp model space, which allow up to five particles to be excited across the shell gap at particle number $N = Z = 28$, successfully describe the excitation scheme, including branching and mixing ratios and a few lifetimes. At high spin and medium-to-high excitation energy it has been possible to follow the evolution of shapes from spherical to moderately deformed, to well deformed shapes throughout the level scheme by comparing the measured quantities to a large set of cranked Nilsson Strutinsky calculations. Consistent configuration assignments have been achieved. Of special interest are the M-1, M-2, M-3, and M-4 structures since they make of ^{60}Ni the lightest system in which magnetic rotation has been observed up to date. The mechanism to produce high-spin states in these structures has similarities with the shears bands in the lead region [18] where the coupling between a proton angular momentum vector \vec{J}^π (which arises from particles in the $1h_{9/2}$ and $1i_{13/2}$ orbitals) and a neutron angular momentum vector \vec{J}^ν (from holes in the $1i_{13/2}$ orbital) generates high angular momentum by aligning J^π and J^ν

in a way that resembles the closing of the blades of a pair of shears. In the present case the bands were described by the coupling between two angular momentum components, a large component created by the collective rotation around a principal axis of the potential, and a small component produced by the $1f_{7/2}$ proton-hole which is perpendicular to the main spin axis; high-spin states in the band are created by the alignment of the latter component with the main spin axis, whereas the neutron and proton $1g_{9/2}$ particles act as spectators in the creation of high-spin states. Thus, in this sense, only one of the blades of the shears is responsible for the production of higher angular momentum states. On the other hand, ^{60}Ni adds to the possibility of consistently refining the Nilsson parameters in the $A \sim 60$ region [59].

ACKNOWLEDGMENTS

We would like to thank the staff and the accelerator crew at ANL and LBNL and also D. P. Balamuth, M. Devlin, J. Eberth, A. Galindo-Uribarri, P. A. Hausladen, L. L. Riedinger, and Th. Steinhardt for the help and support during the experiments. This research was supported in part by the Instituto Colombiano para el Avance de la Ciencia (Colciencias) and the Swedish Institute (D. A. Torres), the Swedish Research Council, and the U.S. DOE grant DE-AC05-000R22725.

-
- [1] C. Andreoiu *et al.*, *Eur. Phys. J. A* **14**, 317 (2002).
 - [2] C. E. Svensson *et al.*, *Phys. Rev. Lett.* **80**, 2558 (1998).
 - [3] C. E. Svensson *et al.*, *Phys. Rev. Lett.* **79**, 1233 (1997).
 - [4] D. Rudolph *et al.*, *Phys. Rev. Lett.* **80**, 3018 (1998).
 - [5] D. Rudolph *et al.*, *Eur. Phys. J. A* **14**, 137 (2002).
 - [6] D. Rudolph *et al.*, *Phys. Rev. Lett.* **89**, 022501 (2002).
 - [7] D. Rudolph *et al.*, *Phys. Rev. Lett.* **82**, 3763 (1999).
 - [8] E. K. Johansson *et al.*, *Phys. Rev. C* **77**, 064316 (2008).
 - [9] D. Rudolph, C. Baktash, M. Devlin, D. R. LaFosse, L. L. Riedinger, D. G. Sarantites, and C. H. Yu, *Phys. Rev. Lett.* **86**, 1450 (2001).
 - [10] C. E. Svensson *et al.*, *Phys. Rev. Lett.* **82**, 3400 (1999).
 - [11] C. Andreoiu *et al.*, *Phys. Rev. Lett.* **91**, 232502 (2003).
 - [12] D. Rudolph *et al.*, *Phys. Rev. Lett.* **96**, 092501 (2006).
 - [13] A. Galindo-Uribarri *et al.*, *Phys. Lett.* **B422**, 45 (1998).
 - [14] D. Karlgren *et al.*, *Phys. Rev. C* **69**, 034330 (2004).
 - [15] S. Frauendorf, *Rev. Mod. Phys.* **73**, 463 (2001).
 - [16] S. Frauendorf, *Z. Phys. A* **358**, 163 (1997).
 - [17] Amita, A. K. Jain, and B. Singh, *At. Data Nucl. Data Tables* **74**, 283 (2000).
 - [18] R. M. Clark and A. O. Macchiavelli, *Annu. Rev. Nucl. Part. Sci.* **50**, 1 (2000).
 - [19] S. Raman, X. Ouyang, M. A. Islam, J. W. Starnes, E. T. Jurney, J. E. Lynn, and G. Martinez-Pinedo, *Phys. Rev. C* **70**, 044318 (2004).
 - [20] D. Cutoi *et al.*, *JYFL Annual Report No. 1991* (1992), p. 58.
 - [21] Yu. G. Kosyakov, D. K. Kaipov, and L. V. Chekushina, *Bull. Acad. Sci. USSR, Phys. Ser.* **53**, 68 (1989).
 - [22] T. U. Chan, C. Morand, F. Azgui, M. Agard, J. F. Bruandet, B. Chambon, A. Dauchy, D. Drain, A. Giorni, and F. Glasser, *Phys. Rev. C* **29**, 441 (1984).
 - [23] F. Kearns *et al.*, *J. Phys. G* **6**, 1131 (1980).
 - [24] H. Ronsin, P. Beuzit, J. Delaunay, R. Ballini, I. Fodor, and J. P. Fouan, *Nucl. Phys.* **A207**, 577 (1973).
 - [25] I.-Y. Lee, *Nucl. Phys.* **A520**, 641c (1990).
 - [26] D. A. Torres, Ph.D. thesis, Universidad Nacional de Colombia (2007).
 - [27] C. E. Svensson *et al.*, *Nucl. Instrum. Methods Phys. Res. A* **396**, 228 (1997).
 - [28] D. G. Sarantites *et al.*, *Nucl. Instrum. Methods Phys. Res. A* **530**, 473 (2004).
 - [29] E. K. Johansson, Licenciante thesis, Lund University, LUNFD6/(NFFR-3099)/1-74 (2006).
 - [30] D. G. Sarantites *et al.*, *Nucl. Instrum. Methods Phys. Res. A* **381**, 418 (1996).
 - [31] D. Seweryniak, J. Nyberg, C. Fahlander, and A. Johnson, *Nucl. Instrum. Methods Phys. Res. A* **340**, 353 (1994).
 - [32] D. C. Radford, *Nucl. Instrum. Methods Phys. Res. A* **361**, 297 (1995).
 - [33] J. Theuerkauf, S. Esser, S. Krink, M. Luig, N. Nicolay, O. Stuch, and H. Wolters, program Tv, University of Cologne, unpublished.
 - [34] C. J. Chiara *et al.*, (to be published).
 - [35] K. S. Krane, R. M. Steffen, and R. M. Wheeler, *At. Data Nucl. Data Tables* **11**, 351 (1973).
 - [36] H. J. Rose and D. Brink, *Rev. Mod. Phys.* **39**, 306 (1967).
 - [37] D. Rudolph *et al.*, *Eur. Phys. J. A* **4**, 115 (1999).
 - [38] J. K. Tuli, *Nucl. Data Sheets* **100**, 347 (2003).
 - [39] E. Caurier, G. Martínez Pinedo, F. Nowacki, A. Poves, and A. P. Zukers, *Rev. Mod. Phys.* **77**, 427 (2005).
 - [40] E. Caurier, Shell model code ANTOINE, IRES, Strasbourg (1989–2002).

- [41] M. Honma, T. Otsuka, B. A. Brown, and T. Mizusaki, *Phys. Rev. C* **65**, 061301(R) (2002).
- [42] M. Honma, T. Otsuka, B. A. Brown, and T. Mizusaki, *Phys. Rev. C* **69**, 034335 (2004).
- [43] A. Poves *et al.*, *Nucl. Phys.* **A694**, 157 (2001).
- [44] R. du Rietz *et al.*, *Phys. Rev. Lett.* **93**, 222501 (2004).
- [45] D. Rudolph, K. P. Lieb, and H. Grawe, *Nucl. Phys.* **A597**, 298 (1996).
- [46] J. Ljungvall, A. Gorgen, M. Girod, J.-P. Delaroche, A. Dewald, C. Dossat, E. Farnea, W. Korten, B. Melon, R. Menegazzo *et al.*, *Phys. Rev. Lett.* **100**, 102502 (2008).
- [47] P. Petkov, A. Dewald, O. Möller, B. Saha, A. Fitzler, K. Jessen, D. Tonev, T. Klug, S. Heinze, J. Jolie *et al.*, *Phys. Rev. C* **68**, 034328 (2003).
- [48] A. Afanasjev, D. Fossan, G. Lane, and I. Ragnarsson, *Phys. Rep.* **322**, 1 (1999).
- [49] T. Bengtsson and I. Ragnarsson, *Nucl. Phys.* **A436**, 14 (1985).
- [50] B. G. Carlsson and I. Ragnarsson, *Phys. Rev. C* **74**, 011302(R) (2006).
- [51] I. Ragnarsson, V. P. Janzen, D. B. Fossan, N. C. Schmeing, and R. Wadsworth, *Phys. Rev. Lett.* **74**, 3935 (1995).
- [52] V. M. Strutinsky, *Nucl. Phys.* **A95**, 420 (1967).
- [53] K. Pomorski and J. Dudek, *Phys. Rev. C* **67**, 044316 (2003).
- [54] K. T. R. Davies and J. R. Nix, *Phys. Rev. C* **14**, 1977 (1976).
- [55] A. V. Afanasjev, I. Ragnarsson, and P. Ring, *Phys. Rev. C* **59**, 3166 (1999).
- [56] M. Zalewski, W. Satuła, W. Nazarewicz, G. Stoitcheva, and H. Zduczuk, *Phys. Rev. C* **75**, 054306 (2007).
- [57] B. G. Carlsson and I. Ragnarsson, *Phys. Rev. C* **74**, 044310 (2006).
- [58] A. Bohr and B. R. Mottelsson, *Nuclear Structure*, Vol. II (W. A. Benjamin, Inc., New York, 1975).
- [59] L.-L. Andersson *et al.*, *Eur. Phys. J. A* **36**, 251 (2008).